Magnetic damping of jet flows in quasi-two-dimensional Rayleigh-Bénard convection

Ashna Aggarwal* and Jonathan M. Aurnou
Department of Earth, Planetary, and Space Sciences, University of California, Los Angeles, California 90095, USA

Susanne Horn
Centre for Fluid and Complex Systems, Coventry University, Coventry CV1 5FB, United Kingdom

(Received 1 March 2022; accepted 12 August 2022; published 13 October 2022)

The mechanism responsible for the damping of the large-scale, azimuthally directed jets observed at Jupiter's surface is not well known, but electromagnetic forces are suspected to play a role as the planet's electrical conductivity increases radially with depth. To isolate the jet damping process, we carry out a suite of direct numerical simulations of quasi-two-dimensional, horizontally periodic Rayleigh-Bénard convection with stress-free boundary conditions in the presence of an external, vertical magnetic field. Jets, punctuated by intermittent convective bursts, develop at Rayleigh numbers (Ra, ratio of buoyancy to diffusion) beyond 10^5 when the magnetic field is relatively weak. Five primary flow regimes are found by varying $10^3 \leqslant \mathrm{Ra} \leqslant 10^{10}$ and the Chandrasekhar number (Ch, ratio of Lorentz to viscosity) $0 \leqslant \mathrm{Ch} \leqslant 10^6$: (i) steady convection rolls, (ii) steady magneto-columns, (iii) unsteady to turbulent magneto-plumes, (iv) horizontally drifting magneto-plumes, and (v) jets with intermittent turbulent convective bursts. We parse the parameter space using transitions derived from the interaction parameter (N, ratio of Lorentz to inertia). The transition to the regime dominated by jets has the most immediate applications to the magnetic damping of Jovian jet flows, where the separation between jets and a magnetically constrained system occurs at a jet-based interaction parameter value of $N_J \approx 1$. We approximate the value of the Jovian interaction parameter as a function of depth, and find that the jets may brake at ≈6000 km below the surface, which is deeper than recent estimates from NASA's Juno mission. This suggests that mechanisms in addition to electromagnetic forces are likely required to fully truncate the jets.

DOI: 10.1103/PhysRevE.106.045104

I. INTRODUCTION

Turbulent flows in planetary and stellar interiors, often driven by convection, are controlled by the complex interplay of stratification, rotation, and magnetic forces. One canonical setup used to understand the fundamental processes behind such flows is Rayleigh-Bénard convection (RBC), in which a fluid is heated from below and cooled from above. RBC studies also often include additional forces such as rotation or an applied magnetic field to gain further insight into geophysical and astrophysical flows [1–10].

Zonal winds, or azimuthally directed large-scale flows (also called "jets"), are one type of flow structure often observed in planetary and stellar systems, such as at the surfaces of Jupiter and Saturn [11–14]. On these planets, the electrical conductivity increases as a function of spherical radius as the outer hydrodynamic molecular envelope transitions to a liquid metal [15–19]. It is the increase in electrical conductivity, and thus electromagnetic effects, that may act as a resistive brake on the azimuthally directed zonal flows through a mechanism known as "magnetic braking." Furthermore, the fundamental question of electromagnetic impact on large-scale flows is relevant to a variety of other systems, including the solar tachocline [20–22] and plasmas in tokamaks [23,24].

Magnetic braking is a magnetohydrodynamic (MHD) phenomenon in which a strong magnetic field suppresses motions in a conducting fluid [25]. In the braking process, motion across magnetic field lines induces electric current, which gives rise to Joule dissipation [26]. In turn, Joule dissipation subtracts from the kinetic energy present in the system, thus usually damping the flow speed, though the induction of magnetic field can complicate the damping effect [27]. Zonal flow in the conducting regions of Jupiter and Saturn could also induce current, leading to Joule dissipation and a decrease in total energy available to the zonal winds [28–32]. Thus, constraints on the zonal wind depth have been made [33], but are based on a specific and unconfirmed set of magnetic field and flow configurations [34].

Spherical shell hydrodynamic models of deep convection that reproduce many of the key jet characteristics have been carried out [35,36]. However, the geometry of each model is truncated at the bottom boundary with a free-slip condition. This serves as a proxy for MHD drag, but does not apply friction on the flow as the electromagnetic effects should. Idealized models that include MHD drag can help quantify the interplay between magnetic forces and jets, which can elucidate the jet-truncation mechanism on planets, such as Jupiter.

We leverage the work of Goluskin *et al.* [37], where it was shown that two-dimensional, horizontally periodic Rayleigh-Bénard convection (RBC) with free-slip boundary conditions

*aggarwal01@ucla.edu

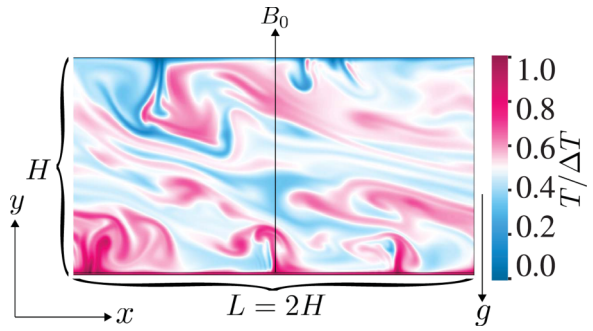

FIG. 1. Instantaneous nondimensional temperature field for a case with zonal jets ($\mathrm{Ra} = 10^8$, $\mathrm{Ch} = 10^2$, $\mathrm{Pr} = 1$, $\Gamma = L/H = 2$, where H is height and L is length of the domain). See Sec. II A for additional parameter definitions. The domain is periodic in the $\hat{\boldsymbol{x}}$ direction, and has fixed temperature and stress-free top and bottom boundary conditions. Gravity points downwards in the negative $\hat{\boldsymbol{y}}$ direction, and a magnetic field is imposed in positive $\hat{\boldsymbol{y}}$ direction, such that $\boldsymbol{B} = B_0\hat{\boldsymbol{y}}$.

can lead to the development of zonal flows, in which the horizontal motion is stronger than the vertical motion by several orders of magnitude. Similar two-dimensional simulations have been carried out by Aubert *et al.* [38], Calkins *et al.* [39], Gastine [40] in rotating annuli or by Scott and Dritschel [41] and Wang *et al.* [42] in a Cartesian domain, producing zonal flows similar to the ones found here. Three-dimensional, rapidly rotating convection simulations in periodic boxes resulting in alternating, unidirectional jets have also been conducted [43,44], as well as rotating spherical shell models with convective bursts [45,46]. Numerous studies have also been carried out to explore the effects of stable stratification on turbulence [47,48], which have implications for the interaction between stable stratification and zonal flows.

Furthermore, rotating convection models have been studied extensively to not only elucidate the process behind planetary zonal flows [31,49–51] but also how planetary magnetic fields are generated and sustained [52–56]. To isolate the MHD braking effects, we consider nonrotating RBC and apply a magnetic field perpendicular to the horizontally directed zonal flows. Figure 1 shows the setup considered in this study for a case with zonal flows in the $\hat{\boldsymbol{x}}$ direction and the magnetic field in the $\hat{\boldsymbol{y}}$ direction. The purpose of this simplified Cartesian model is to investigate the fundamental magnetic damping mechanism in a system where jets are generated self consistently.

The rest of the paper is organized as follows: the governing equations and the numerical methods are given in Sec. II. Section III gives a theoretical framework to separate the regimes based on the properties of the Lorentz force and the interaction parameter. In Sec. IV, we use flow properties such as length scale, momentum transport, and time-dependence to distinguish between the differing flow regimes, and in Sec. V we derive interaction transition laws based on length and velocity data to separate these regimes. We conclude in Sec. VI, and discuss the implications of our results for the depth of zonal winds on Jupiter.

II. GOVERNING EQUATIONS AND NUMERICAL METHODS

We present the framework for understanding MHD flows under the presence of a strong, uniform magnetic field, before introducing the governing equations specific to the setup used here. Configurations with a strong mean magnetic field have been the focus of a number of studies [1,8,57–65]. A simplification often made is to apply the quasistatic approximation (QSA), which states that the induced magnetic field, $\boldsymbol{b}$, is negligible, and $\partial\boldsymbol{b}/\partial t \approx 0$ [25,66–68]. QSA is typically invoked when the magnetic Reynolds number, $Rm = (U\mathcal{L})/\eta$, is significantly lower than 1 (where U is a characteristic velocity scale, $\mathcal{L}$ is a characteristic length scale, and η the magnetic diffusivity). QSA can be used to simplify the Lorentz force

$$\boldsymbol{F}_L = \boldsymbol{j} \times \boldsymbol{B}, \tag{1}$$

where $\boldsymbol{B}$ is the magnetic field and $\boldsymbol{j}$ is the current density. In previous studies this simplification has been done in two different ways: using Ohm's Law to find the current density, which is known as the potential formulation, or by using the induction formulation [64]. We demonstrate here that both frameworks are equivalent, which allows us to utilize the potential formulation to calculate the Lorentz force in our model. We employ the induction formulation to demonstrate the tendency for the Lorentz force to dampen velocity gradients parallel to the magnetic field. This MHD formalism applies to both 3D and 2D setups with a uniform vertical magnetic field defined by

$$\boldsymbol{B} = B_0\hat{\boldsymbol{y}} + \boldsymbol{b}, \tag{2}$$

where $B_0\hat{\boldsymbol{y}}$ is the applied field and $\boldsymbol{b}$ is the induced field.

A. Potential formulation

The Lorentz force is given by Eq. (1). We can use Faraday's Law to write the electric field $\boldsymbol{E}$ in terms of the magnetic vector potential $\boldsymbol{A}$,

$$\nabla \times \boldsymbol{E} = -\frac{\partial}{\partial t}\boldsymbol{B} = \frac{\partial}{\partial t}(\nabla \times \boldsymbol{A}) = 0, \tag{3}$$

which gives an equation for the electric field

$$\boldsymbol{E} = -\nabla\phi - \frac{\partial}{\partial t}\boldsymbol{A}. \tag{4}$$

Under QSA, $\partial\boldsymbol{A}/\partial t = 0$. Thus, the electric field can be expressed purely using a scalar potential, ϕ,

$$\boldsymbol{E} = -\nabla\phi. \tag{5}$$

Using Ohm's Law for the current density and taking its curl yields

$$\nabla \times \boldsymbol{j} = \sigma B_0 \frac{\partial \boldsymbol{u}}{\partial y}, \tag{6}$$

where $\boldsymbol{u}$ is the fluid velocity and σ is the electrical conductivity. Taking the curl of the curl of Eq. (1), the gradient of the divergence of Eq. (1), and using Eq. (6) allows us to express the Lorentz force as

$$\nabla^2\boldsymbol{F}_L = \nabla\left(\sigma B_0^2 \frac{\partial u_y}{\partial y}\right) - \sigma B_0^2\left(\frac{\partial^2 \boldsymbol{u}}{\partial y^2}\right). \tag{7}$$

B. Induction formulation

We define the current density by

$$\boldsymbol{j} = \frac{1}{\mu}(\nabla \times \boldsymbol{B}). \tag{8}$$

The Lorentz force density (1) becomes

$$\boldsymbol{F_L} = \frac{1}{\mu}(\nabla \times \boldsymbol{B} \times \boldsymbol{B}) = -\nabla\left(\frac{1}{2\mu}\boldsymbol{B}^2\right) + \frac{1}{\mu}(\boldsymbol{B}\cdot\nabla)\boldsymbol{B}. \tag{9}$$

Equation (9) can be simplified by substituting $\boldsymbol{B} = B_0\hat{\boldsymbol{y}} + \boldsymbol{b}$ and neglecting terms $\mathcal{O}(\boldsymbol{b}^2)$ to give

$$\boldsymbol{F_L} = -\nabla\left(\frac{1}{\mu}B_0 b_y\right) + \frac{1}{\mu}\left(B_0\frac{\partial \boldsymbol{b}}{\partial y}\right). \tag{10}$$

The first term on the right-hand side of Eq. (10) is irrotational and represents a magnetic pressure [66]. The second term is the rotational component of the Lorentz force. Under QSA with a uniform vertical magnetic field, the magnetic induction equation reduces to

$$B_0\frac{\partial \boldsymbol{u}}{\partial y} = -\eta\nabla^2\boldsymbol{b}. \tag{11}$$

Solving Eq. (11) for the induced field, $\boldsymbol{b}$, gives

$$\boldsymbol{b} = -\frac{B_0}{\eta}\Delta^{-1}\frac{\partial \boldsymbol{u}}{\partial y}, \tag{12}$$

where Δ^{-1} is the inverse Laplacian operator. The Lorentz force simplifies to

$$\boldsymbol{F_L} = \nabla\left(\frac{B_0^2}{\mu\eta}\Delta^{-1}\frac{\partial u_y}{\partial y}\right) - \frac{B_0^2}{\mu\eta}\Delta^{-1}\frac{\partial^2 \boldsymbol{u}}{\partial y^2}. \tag{13}$$

Taking the Laplacian of both sides, we find

$$\nabla^2\boldsymbol{F_L} = \nabla\left(\sigma B_0^2\frac{\partial u_y}{\partial y}\right) - \sigma B_0^2\left(\frac{\partial^2 \boldsymbol{u}}{\partial y^2}\right), \tag{14}$$

where $\sigma = 1/(\mu\eta)$. This is identical to Eq. (7), which shows that the potential formulation and the induction formulation for the current density yield the same Lorentz force. We observe an important characteristic of the Lorentz force under QSA. Namely, following Eq. (13), the Lorentz force tends to dampen velocity gradients parallel to the magnetic field [58,64,68–70].

Next, we present the quasi-2D Cartesian Navier-Stokes equations for Rayleigh-Bénard convection (RBC) under the Oberbeck-Boussinesq approximation. We include a quasistatic magnetic field parallel to the direction of buoyancy. The horizontally periodic domain has stress-free velocity boundary conditions and fixed temperature boundary conditions. The dimensional governing equations for the velocity $\boldsymbol{u}(x, y, t)$ and temperature $T(x, y, t)$ fields are

$$\nabla\cdot\boldsymbol{u} = 0, \tag{15}$$

$$\nabla\cdot\boldsymbol{B} = 0, \tag{16}$$

$$\frac{\partial \boldsymbol{u}}{\partial t} + (\boldsymbol{u}\cdot\nabla)\boldsymbol{u} = -\frac{1}{\rho_0}\nabla p + \alpha g(T - T_0)\hat{\boldsymbol{y}} + \nu\nabla^2\boldsymbol{u} + \frac{1}{\rho_0}(\boldsymbol{j}\times\boldsymbol{B}), \tag{17}$$

$$\frac{\partial T}{\partial t} + (\boldsymbol{u}\cdot\nabla)T = \kappa\nabla^2 T, \tag{18}$$

where where $\boldsymbol{u}$ is the fluid velocity, p is the pressure, ρ_0 is the constant mass density, α is the coefficient of thermal expansion, g is gravitational acceleration, T_0 is the reference temperature, ν is the viscosity, and κ is the thermal diffusivity.

In the quasi-2D configuration, forces are permitted in the third, $\hat{\boldsymbol{z}}$ direction, though $\boldsymbol{u}$ and T remain independent of z. Furthermore, we apply the additional condition, $u_z = 0$. This allows us to calculate the cross-product of the Lorentz term in Eq. (17). The Lorentz force density, $\boldsymbol{f_L}$, is given by

$$\boldsymbol{f_L} = \frac{\boldsymbol{F_L}}{\rho_0} = \frac{1}{\rho_0}(\boldsymbol{j}\times\boldsymbol{B}). \tag{19}$$

We can apply the potential formulation (3)–(5) in this quasi-2D setup to find

$$\boldsymbol{f_L} = \frac{\sigma}{\rho_0}((\boldsymbol{u}\times\boldsymbol{B})\times\boldsymbol{B}) = -\frac{\sigma B_0^2}{\rho_0}u_x\hat{\boldsymbol{x}}. \tag{20}$$

Equations (15)–(18) are integrated in the vorticity-stream function formulation. The vorticity, $\boldsymbol{\omega}$, is defined as the curl of the velocity field, where

$$\boldsymbol{\omega} = \nabla\times\boldsymbol{u} = \omega_z\hat{\boldsymbol{z}}. \tag{21}$$

The stream function ψ can be used to describe the velocity field via

$$u_x = -\frac{\partial}{\partial y}\psi,\ u_y = \frac{\partial}{\partial x}\psi = -\omega_z. \tag{22}$$

The vorticity is related to the stream function with

$$\nabla^2\psi = -\omega_z. \tag{23}$$

The vorticity evolution equation is found by taking the curl of Eq. (17). Since all the terms in the vorticity equation are in the z direction, the scalar vorticity equation for the $\hat{\boldsymbol{z}}$ component is

$$\frac{\partial\omega}{\partial t} + (\boldsymbol{u}\cdot\nabla)\omega = \alpha g\frac{\partial T}{\partial x} + \nu\nabla^2\omega + \frac{\sigma B_0^2}{\rho_0}\frac{\partial^2\psi}{\partial y^2}, \tag{24}$$

where we have set $\omega \equiv \omega_z$.

C. Numerical method

The approach used to numerically solve the governing equations in the direct numerical simulations (DNS) is given here. First, to nondimensionalize the system, the length is scaled by the height of the domain, H; time by the free-fall timescale, $\tau_{\mathrm{ff}} = H/\sqrt{\alpha g\Delta T}$; temperature by the temperature difference from the hot bottom to the cold top boundary in the static state, ΔT; and magnetic field by B_0. Under these scales the free-fall velocity is given by

$$u_{\mathrm{ff}} = \sqrt{\alpha g\Delta T H}. \tag{25}$$

The quasi-2D nondimensional equations for quasistatic magnetoconvection in the vorticity-stream function formulation are

$$\frac{\partial \omega}{\partial t} + (\boldsymbol{u}\cdot\boldsymbol{\nabla})\omega = \frac{\partial T}{\partial x} + \sqrt{\frac{\mathrm{Pr}}{\mathrm{Ra}}}\nabla^2\omega + \sqrt{\frac{\mathrm{Ch}^2\mathrm{Pr}}{\mathrm{Ra}}}\frac{\partial^2\psi}{\partial y^2}, \quad (26)$$

$$\frac{\partial T}{\partial t} + (\boldsymbol{u}\cdot\boldsymbol{\nabla})T = \frac{1}{\sqrt{\mathrm{Ra}\,\mathrm{Pr}}}\nabla^2 T, \quad (27)$$

along with (23) and (22). The Rayleigh number (Ra, ratio of buoyancy to diffusion), Prandtl number (Pr, ratio of viscous to thermal diffusion), and Chandrasekhar number (Ch, ratio of Lorentz to viscosity) are given by

$$\mathrm{Ra} = \frac{\alpha g \Delta T H^3}{\nu\kappa}, \ \mathrm{Pr} = \frac{\nu}{\kappa}, \ \mathrm{Ch} = \frac{\sigma B_0^2 H^2}{\rho_0 \nu}. \quad (28)$$

The aspect ratio of our horizontally periodic domain is defined by $\Gamma = L/H$ where L is the length and H is the height. We vary $10^3 \leqslant \mathrm{Ra} \leqslant 10^{10}$ and $0 \leqslant \mathrm{Ch} \leqslant 10^6$. For most cases, we fix $\mathrm{Pr} = 1$. A discussion of magnetic braking at varying Prandtl is given in Sec. V A.

Wang *et al.* [42] carried out a comprehensive study of zonal flow dependence on Γ in horizontally periodic 2D RBC with stress-free and isothermal top and bottom boundary conditions. It was shown that zonal flows cannot be sustained when Γ is larger than a critical value that also depends on Ra, Pr. Both Wang *et al.* [42] and Goluskin *et al.* [37] found that zonal flows develop readily at $\Gamma = 2$ when $\mathrm{Ch} = 0$. Thus, we choose to fix $\Gamma = 2$ for this study that seeks to isolate the magnetic damping mechanism on zonal flows.

Our main output parameters are the Nusselt number, Nu, which defines the heat transfer across the layer, and the Reynolds number, Re, which defines the momentum transport. The Nusselt number is

$$\mathrm{Nu} = 1 + \frac{H\langle u_y T\rangle_{x,y}}{\kappa\Delta T}, \quad (29)$$

where $\langle\rangle_{x,y}$ refers to the area average. The Reynolds number is

$$\mathrm{Re} = \frac{UH}{\nu}, \quad (30)$$

where U is a characteristic velocity scale. In particular, we will measure

$$\mathrm{Re}_x = \frac{\langle|u_x|\rangle_{x,y}H}{\nu}, \ \mathrm{Re}_y = \frac{\langle|u_y|\rangle_{x,y}H}{\nu}. \quad (31)$$

We have developed an MPI parallelized, pseudo-spectral solver that numerically integrates the governing Eqs. (26) and (27) at each time step. It first calculates the linear terms of Eqs. (26) and (27). Then it transforms the solution to physical space to calculate the nonlinear terms, updates the temperature field and vorticity field, and solves the Poisson equation for the stream function based on the vorticity field. Finally, it updates the velocity field. The code utilizes M Fourier modes in the periodic x direction and solves the resulting equations for each Fourier mode m using a second-order accurate finite difference scheme in y [71].

The grid-spacing is nonuniform with Chebyshev mapping for finer resolution at the top and bottom boundaries defined by

$$y_k = \frac{1}{2}\left[1 - \cos\left(\frac{k\pi}{n_y}\right)\right] \text{ for } k = 1, ...n_y, \quad (32)$$

where y_k is vertical location at each grid point k and n_y is the total number of vertical grid points [71]. The nonlinear terms are calculated using a spectral-transform method, and the solution is advanced in time using a second-order Adams-Bashforth time integration scheme.

The open-source pseudospectral DNS code DEDALUS [72] is used to carry out the most numerically challenging cases with turbulent intermittent convective bursts ($\mathrm{Ra} \geqslant 10^9$). Both codes are benchmarked to Goluskin *et al.* [37], as shown in Appendix B.

D. Marginal stability analysis

Marginal stability analysis for magnetoconvection with a uniform vertical magnetic field and stress-free, isothermal vertical boundary conditions has been carried out by Glatzmaier [71] and Chandrasekhar [73]. We follow these studies to find $\mathrm{Ra}_{\mathrm{mar}}$, the marginally unstable Rayleigh number as a function of aspect ratio and horizontal Fourier mode number, m,

$$\mathrm{Ra}_{\mathrm{mar}}(m, \mathrm{Ch}, \Gamma) = \pi^2\mathrm{Ch}\left[\frac{(\Gamma^2 + m^2)}{m^2}\right] + \pi^4\left[\frac{(\Gamma^2 + m^2)^2}{\Gamma^4 m^2}\right]. \quad (33)$$

We have assumed that structures that extend from bottom to top of the box are the most unstable such that the vertical mode number is equal to 1. The critical horizontal mode number, m_c, found by setting the derivative of Eq. (33) with respect to m to zero, is given by

$$m_c = \Gamma\sqrt{\frac{\chi^{4/3} + \pi^{4/3} - (\pi\chi)^{2/3}}{2(\pi\chi)^{2/3}}}, \quad (34)$$

where

$$\chi = \sqrt{\mathrm{Ch}} + \sqrt{\mathrm{Ch} + \pi^2}. \quad (35)$$

Substituting Eq. (34) into Eq. (33) gives the critical Rayleigh number, $\mathrm{Ra}_c(\mathrm{Ch})$. If Ch is too large at a given Ra such that $\mathrm{Ra} < \mathrm{Ra}_c$, then convection is suppressed, and at $\mathrm{Ra} = \mathrm{Ra}_c$ magnetoconvection motions begin.

In the hydrodynamic limit where $\mathrm{Ch} = 0$, Eq. (33) becomes the well-known relationship [71,73]

$$\mathrm{Ra}_{\mathrm{mar}}(m, \mathrm{Ch} = 0, \Gamma) = \pi^4\left[\frac{(\Gamma^2 + m^2)^2}{\Gamma^4 m^2}\right]. \quad (36)$$

Following Eq. (36), the Rayleigh number is minimal for $\Gamma = \sqrt{2}$, where $m_c = 1$ and $\mathrm{Ra}_c = 657.5$, which is also the infinite plane layer solution [73].

In the limit $\mathrm{Ch} \to \infty$,

$$m_c^\infty \to \Gamma\left(\frac{\mathrm{Ch}}{2\pi^2}\right)^{1/6}, \quad (37)$$

and

$$\mathrm{Ra}_c^\infty \to \pi^2\mathrm{Ch}, \quad (38)$$

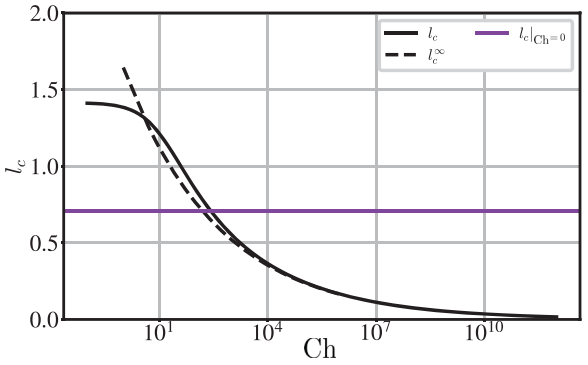

FIG. 2. The critical horizontal length scale l_c as predicted by planar linear theory. The solid black line gives the length scale following Eq. (41), and the solid purple line gives the result of Eq. (41) for $\mathrm{Ch} = 0$, the hydrodynamic case. The black dashed line shows the asymptotic behavior given by Eq. (42).

in agreement with Refs. [62,71,73–75]. The critical horizontal wave number is given by

$$k_c = \frac{\pi m_c}{\Gamma}. \tag{39}$$

Using k_c, the critical horizontal wavelength λ_c is inversely related to m_c by

$$\lambda_c = \frac{2\pi}{k_c} = \frac{2\Gamma}{m_c}, \tag{40}$$

The critical length scale of the convective structures, or half the wavelength, is given by

$$l_c = \frac{\Gamma}{m_c}. \tag{41}$$

In the limit of $\mathrm{Ch} \to \infty$, l_c^∞ is given by

$$l_c^\infty = \left(\frac{\mathrm{Ch}}{2\pi^2}\right)^{-1/6}. \tag{42}$$

Figure 2 shows l_c and its asymptotic behavior as $\mathrm{Ch} \to \infty$. Length scales found in this study will be compared to these values, where m_c is taken to the nearest integer.

III. THE INTERACTION PARAMETER

The magnetic field modifies convection by changing the dominant perpendicular length scale and suppressing flow perpendicular to the applied field. The underlying theory relies on one of the most notable characteristics of magnetohydrodynamics: the ability for flows to generate electrical currents. The currents lead to Joule dissipation, which in addition to viscous dissipation, contributes to the total energy loss in the system [26,68,76].

Joule dissipation plays a key role in the magnetic braking process and has been discussed in depth in previous studies [58,64,68,70]. To demonstrate how the Lorentz force results in Joule dissipation, we first separate the Lorentz force into rotational and irrotational components. We can absorb the irrotational component into the reduced pressure [70], which leaves only the rotational component of the Lorentz force in Eq. (13),

$$\boldsymbol{f}_{\boldsymbol{L},\boldsymbol{R}} = -\frac{\sigma B_0^2}{\rho_0}\Delta^{-1}\frac{\partial^2 \boldsymbol{u}}{\partial y^2}. \tag{43}$$

The vorticity Eq. (24) can be rewritten to include the curl of Eq. (43),

$$\frac{\partial \omega}{\partial t} + (\boldsymbol{u}\cdot\boldsymbol{\nabla})\omega = \alpha g\frac{\partial T}{\partial x} + \nu\nabla^2\omega - \frac{\sigma B_0^2}{\rho_0}\Delta^{-1}\frac{\partial^2\omega}{\partial y^2}. \tag{44}$$

Assuming that the viscous and Lorentz terms of Eq. (44) are in balance with the unsteady term, we have

$$\frac{\partial \omega}{\partial t} = \nu\nabla^2\omega - \frac{\sigma B_0^2}{\rho_0}\Delta^{-1}\frac{\partial^2\omega}{\partial y^2}. \tag{45}$$

Local viscous and Joule dissipation timescales can be estimated using Eq. (45). We estimate the gradients as

$$\frac{\partial^2}{\partial y^2} \sim \frac{1}{l_\parallel^2}, \quad \frac{\partial^2}{\partial x^2} \sim \frac{1}{l_\perp^2}, \tag{46}$$

where the subscripts $\parallel$ and $\perp$ denote quantities parallel and perpendicular to the direction of the applied magnetic field respectively. The vorticity ω will then decay on one of two timescales. The viscous timescale is $\tau_\nu = l_\parallel^2/\nu$ according to the first term on the right-hand side of Eq. (45). The Joule dissipation timescale, τ_j is given by the second term on the right-hand side of Eq. (45). Thus, for a given eddy of size $\Delta^{-1} \sim l_\perp^2$, the Lorentz term can be thought of as a diffusion term similar to the viscous term [58]. The Joule dissipation timescale can be written as

$$\tau_j = \frac{\rho_0}{\sigma B_0^2}\left(\frac{l_\parallel}{l_\perp}\right)^2, \tag{47}$$

where the dominant term from Δ^{-1} reduces to $l_\perp^2$ under the assumption that gradients parallel to the magnetic field have been suppressed. Taking the ratio of Eq. (47) to an eddy turnover time, $\tau_U = l_\perp/U$ leads to a local interaction parameter

$$N_l = \frac{\tau_U}{\tau_j} = \frac{\sigma B_0^2 l_\perp}{\rho_0 U}\left(\frac{l_\perp}{l_\parallel}\right)^2. \tag{48}$$

Equation (48) has been shown to capture the Lorentz force relative to inertia in experimental studies of MHD channel flows [70,77]. Rewriting Eq. (48) in terms of Ch, Re, which will be utilized in Sec. V, gives

$$N_l = \frac{\mathrm{Ch}}{\mathrm{Re}}\left(\frac{l_\perp}{H}\right)^3. \tag{49}$$

In cases where flow gradients parallel to the magnetic field are not suppressed and $l_\perp \sim l_\parallel$, Eq. (47) reduces to

$$\tau_j = \frac{\rho_0}{\sigma B_0^2}. \tag{50}$$

Comparing this simplified Joule dissipation time to an eddy turnover time leads to the large-scale interaction parameter

$$N = \frac{\tau_U}{\tau_j} = \frac{\sigma B_0^2 l_\perp}{\rho_0 U} = \frac{\mathrm{Ch}}{\mathrm{Re}}\left(\frac{l_\perp}{H}\right), \tag{51}$$

where $l_\parallel \approx H$. Equations (49) and (51) give two representations of the interaction parameter that can be used to treat the

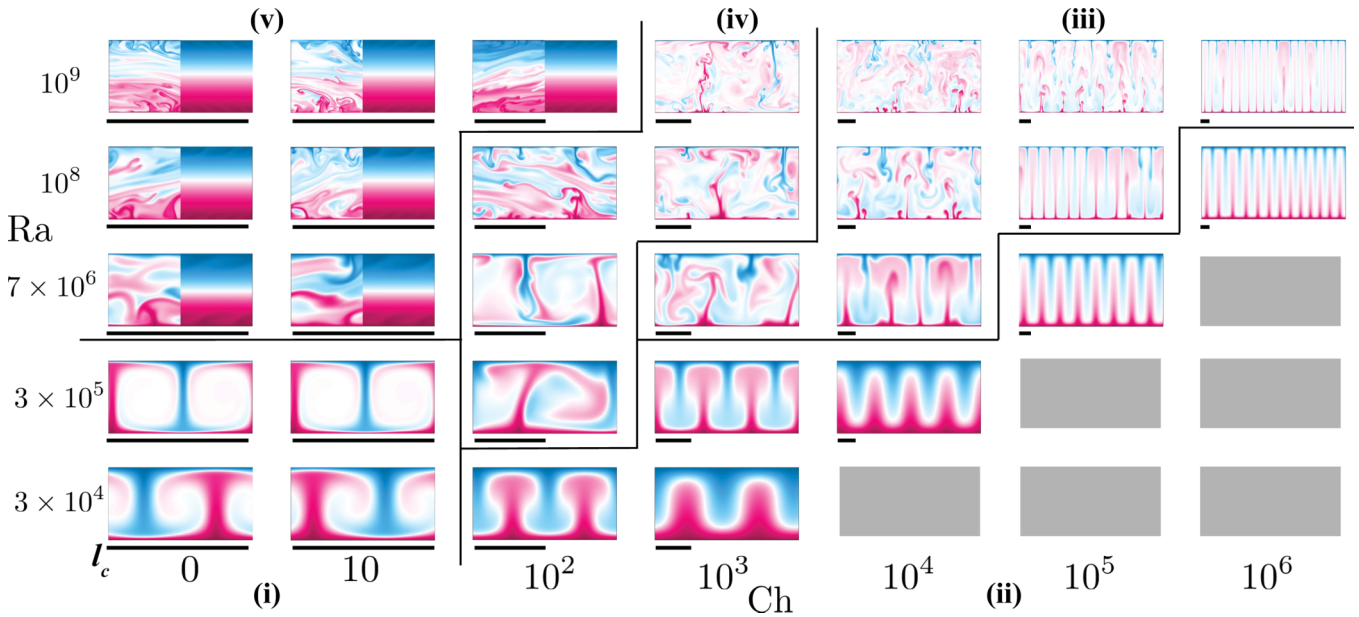

FIG. 3. Instantaneous temperature fields for $10^4 \leqslant \mathrm{Ra} \leqslant 10^9$ and $10 \leqslant \mathrm{Ch} \leqslant 10^6$. The gray boxes are subcritical, while the black lines correspond to regime boundaries. For some cases in the burst-jet regime (v), the left half of the domain shows a snapshot in the convective burst phase (image truncated at $x = \Gamma/2$), and the right half of the domain shows a snapshot in the jet phase (image truncated at $x = \Gamma/2$). The thick black line under each snapshot gives l_c as predicted by Eq. (41) with m_c to the nearest integer.

end-member flows expected in this system. Equation (49) is used for flows controlled by the applied magnetic field B_0 and Eq. (51) for flows with large-scale jets and strong shear in the direction of the magnetic field.

IV. REGIME CHARACTERISTICS

The regimes in this study are distinguished quantitatively by their length scale, momentum transport, and time-dependence. They are

(i) steady convection rolls,

(ii) steady magnetocolumns,

(iii) unsteady to turbulent magnetoplumes ("magnetoplumes"),

(iv) horizontally drifting magnetoplumes ("drifting plumes"),

(v) jets with intermittent turbulent convective bursts ("burst-jet").

These regimes have distinct morphological behaviors similar to those found in prior studies of magnetoconvection [62,78] and rotating convection [7,79–82].

Figure 3 presents instantaneous temperature fields for an array of cases between $3 \times 10^4 \leqslant \mathrm{Ra} \leqslant 10^9$ and $0 \leqslant \mathrm{Ch} \leqslant 10^6$. Cases in the steady convection roll regime (i) have one steady convection roll. The perpendicular length scale of the roll is given by $l_\perp = 1$, and in this regime the strength of the magnetic field relative to buoyancy is small enough such that the weakly nonlinear dynamics characteristic of steady RBC are not drastically modified [10,83,84]. Analysis of a similar 2D RBC system with stress-free horizontal boundaries shows that the steady roll arises through a pitchfork bifurcation [85,86].

Cases in the steady magnetocolumns regime (ii) are characterized by a series of narrow, steady convective columnar structures. The width of these columns closely follows linear theory as predicted by Eq. (41) with m_c to the nearest integer and demonstrated by the thick black line under each snapshot. This regime includes cases that are steady and where $l_\perp < 1$. Similar to RBC, the transition to this stationary regime of magnetoconvection is given by a pitchfork bifurcation [3].

In the magnetoplumes regime (iii), the buoyancy forcing is stronger relative to the Lorentz force. Convective plumes transfer heat efficiently and have a mushroom-like shape [87–90]. The Lorentz force stabilizes the flow, which is approximately aligned with the vertical magnetic field.

In the drifting plume regime (iv), asymmetries exist in the flow field such that convective plumes drift horizontally. However, the horizontal flow is not strong enough to disperse the plumes. Finally, (v) gives cases in the burst-jet regime, which are characterized by two distinct phases. Over the evolution of a case, a period of high heat transport where convective plumes cross the fluid layer ("burst") are interrupted by quiet phases of weak heat transport, where strong zonal flows ("jets") disperse thermal plumes and inhibit convection [91]. The left (right) side of the snapshots corresponds to the burst (jet) phases. As shown in Rucklidge and Matthews [85], Paul *et al.* [86], Cross and Greenside [92], the transitions to these time-periodic flows from the steady regimes are known to occur through a Hopf bifurcation.

Figure 4 shows a time series of the Nusselt number Nu (left column) and a time series of the vertical and horizontal Reynolds numbers, $\mathrm{Re}_y, \mathrm{Re}_x$ (right column). It is used to quantitatively distinguish the regimes from one another. Figure 4(a) shows Nusselt for a case in the steady convection roll regime at $\mathrm{Ra} = 3 \times 10^5$, $\mathrm{Ch} = 10$ where Nu remains constant at 16.30. Figure 4(b) shows the Reynolds numbers for the same case, where the horizontal and vertical Reynolds numbers are nearly equivalent. Figure 4(c) gives

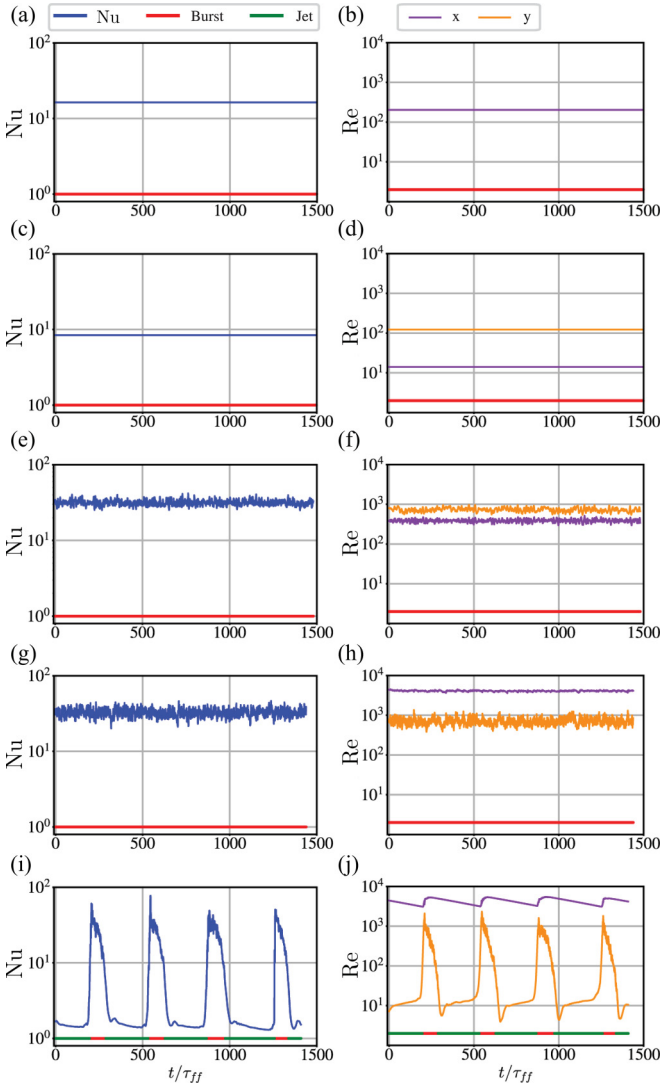

FIG. 4. The left column shows the times series of Nu, and the right column Re_x (purple), Re_y (orange). Each row corresponds to $\mathrm{Ra} = 3 \times 10^5$, $\mathrm{Ch} = 10$ [[(a), (b)] steady convection roll regime], $\mathrm{Ra} = 7 \times 10^6$, $\mathrm{Ch} = 10^6$ [[(c), (d)] magnetocolumns regime], $\mathrm{Ra} = 10^8$, $\mathrm{Ch} = 10^4$ [[(e), (f)] magnetoplume regime], $\mathrm{Ra} = 10^8$, $\mathrm{Ch} = 10^2$ [[(g), (h)] drifting plumes regime], and $\mathrm{Ra} = 10^8$, $\mathrm{Ch} = 10$ [[(i), (j)] burst-jet regime]. In the left column, the green and red markers correspond to points separated into the burst or jet phase based on Eq. (52).

Nusselt for a case in the steady magnetocolumns regime at $\mathrm{Ra} = 7 \times 10^6$, $\mathrm{Ch} = 10^5$ where Nu remains constant at 8.42. Figure 4(d) shows that the vertical Reynolds number exceeds the horizontal Reynolds number, because flows that are perpendicular to the applied vertical magnetic field are damped.

Figures 4(e) and 4(f) show the Nusselt number and Reynolds numbers for a case in the magnetoplumes regime at $\mathrm{Ra} = 10^8$, $\mathrm{Ch} = 10^4$, where small temporal oscillations in each quantity are observed. Furthermore, it is clear from Fig. 4(f) that the vertical Reynolds number exceeds the horizontal Reynolds number. Cases are placed in these regime if they are unsteady or turbulent, and if $\langle \mathrm{Re}_x \rangle_t \leqslant \langle \mathrm{Re}_y \rangle_t$. The unsteadiness of the flow is quantified by the variance of the vertical velocity in time, or $\mathrm{var}(\mathrm{Re}_y)$.

Figures 4(g) and 4(h) show the Nusselt number and Reynolds numbers for a case in the drifting plumes regime at $\mathrm{Ra} = 10^8$, $\mathrm{Ch} = 10^2$. In contrast to the previous regime, the horizontal Reynolds number now exceeds the vertical Reynolds number. Therefore, one characteristic of this regime is that it is unsteady or turbulent, and $\langle \mathrm{Re}_x \rangle_t > \langle \mathrm{Re}_y \rangle_t$.

Figures 4(i) and 4(j) show the Nusselt number and Reynolds numbers for a case in the burst-jet regime at $\mathrm{Ra} = 10^8$, $\mathrm{Ch} = 10$, where strong temporal periodicity is observed in each parameter. We choose to separate the burst and jet phases based on a threshold value of the instantaneous Nusselt number compared to its mean. If

$$\frac{\mathrm{Nu}(t)}{\langle \mathrm{Nu} \rangle_t} < \frac{1}{2}, \tag{52}$$

then the data point is placed in the jet phase; otherwise, it is placed in the burst phase. The time spent in each phase is averaged for each case, yielding values for $t_{\mathrm{jet}}/\tau_{\mathrm{ff}} = \tau_{\mathrm{jet}}$ and $t_{\mathrm{burst}}/\tau_{\mathrm{ff}} = \tau_{\mathrm{burst}}$, respectively. Values of $\tau_{\mathrm{jet}} > 0$ are unique to the burst-jet regime. Therefore, cases are placed in these regime if they are unsteady or turbulent, $\langle \mathrm{Re}_x \rangle_t > \langle \mathrm{Re}_y \rangle_t$, and $\tau_{\mathrm{jet}} > 0$. If $\tau_{\mathrm{jet}} = 0$, then it is placed in the prior drifting plumes regime. Further discussion of the time-averaged Nusselt number in each regime is given in Appendix C.

A. Length and velocity scales

It is necessary to measure perpendicular length scales, $l_\perp$, and velocity scales to find where in (Ra, Ch) parameter space regime transitions occur using interaction parameter arguments.

Figure 5 shows the time average of horizontal spectra where the temperature field has been vertically averaged ($\langle \langle \widetilde{T} \rangle_y (m) \rangle_t$). Here, $\widetilde{T}$ distinguishes the spectra of the temperature from its representation in physical space. An example from each regime is shown. The mode number that corresponds to the spectra peak, m_{peak} is used to calculate $l_\perp = \Gamma/(m_{\mathrm{peak}})$, which is equivalent to the wavelength of a structure in a system with periodic sidewall boundary conditions.

Figure 5(a) gives the spectra for a case in the steady convection roll regime where $m_{\mathrm{peak}} = 1$ corresponds to $l_\perp = 1$. Figure 5(b) gives an example of a case in the steady magnetocolumns regime where $\mathrm{Ch} = 10^6$, $\mathrm{Ra} = 10^8$. The vertical black line denotes the horizontal mode number predicted by linear theory, m_c. The spectral peak, m_{peak}, occurs close to m_c, which shows that the width of the columns is given by $l_\perp \sim \mathrm{Ch}^{-1/6} H$. A similar behavior is found for the magnetoplume regime as given in Fig. 5(c) at $\mathrm{Ch} = 10^5$, $\mathrm{Ra} = 10^9$. The spectral peak, m_{peak} occurs near m_c, again demonstrating that the width of the plumes closely follows $l_\perp \sim \mathrm{Ch}^{-1/6} H$.

Figure 5(d) gives the spectra for a case in the drifting plumes regime at $\mathrm{Ch} = 10^3$, $\mathrm{Ra} = 10^8$. A change in the perpendicular length-scale behavior is observed. There is an increase in m_{peak} relative to m_c. As Ra is increased for a given Ch, the plumes begin to merge and their horizontal width increases. Finally, Fig. 5(e) shows the spectra for a case in the burst-jet regime at $\mathrm{Ch} = 10$, $\mathrm{Ra} = 10^8$, where m_{peak} is 1

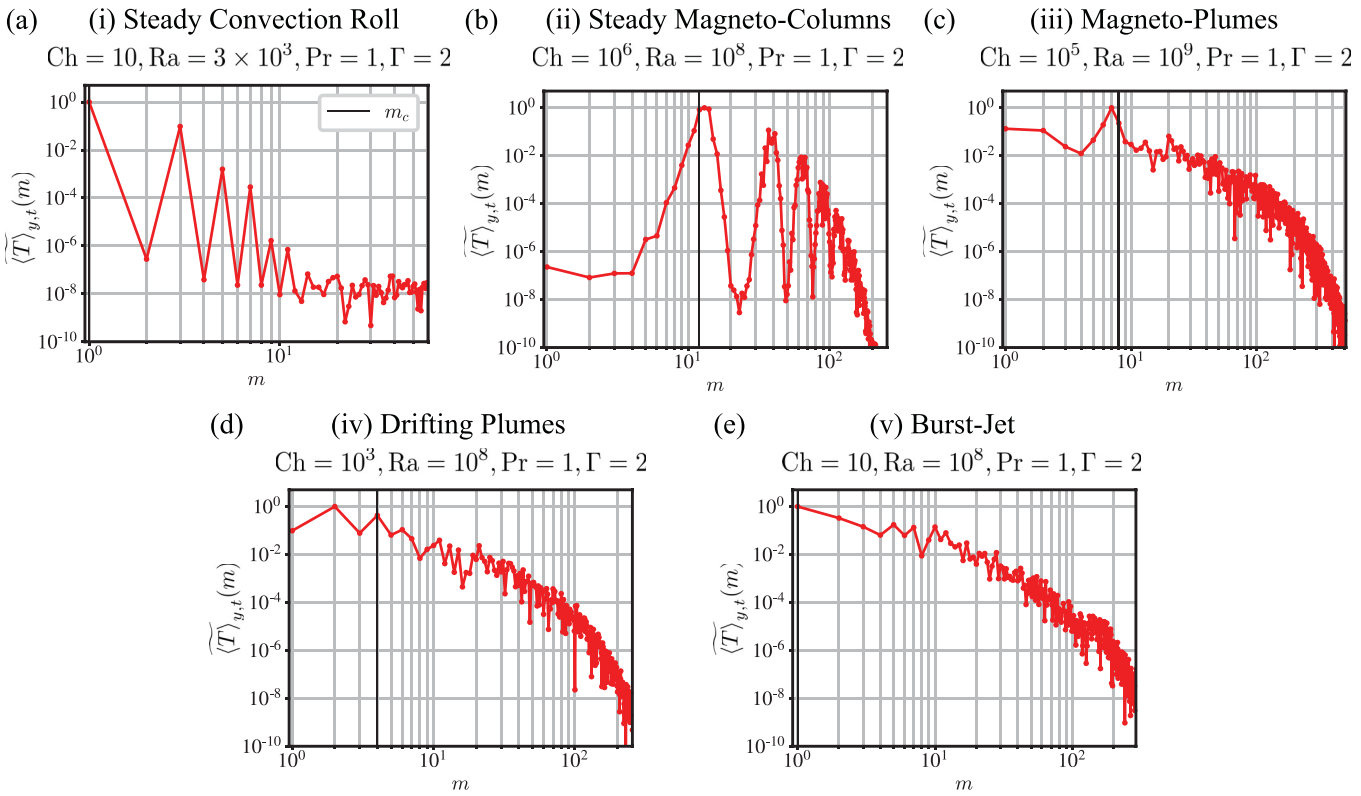

FIG. 5. Examples of spectra ($\langle\langle\widetilde{T}\rangle_y(m)\rangle_t$) from each regime that compare the mode numbers to the spectra peak, m_{peak} to the critical horizontal mode number, m_c, to the nearest integer (denoted by a solid black line). (a) Steady convection roll, (b) steady magnetocolumns, (c) magnetoplumes, (d) drifting plumes, and (e) burst-jet. The measured perpendicular length scale $l_\perp$ is then given by $l_\perp = \Gamma/(2m_{\text{peak}})$ following Eq. (41).

demonstrating that the flow is dominated by the lowest mode numbers.

Figure 6 shows the measured $l_\perp$ normalized by l_c predicted by theory (using m_c rounded to the nearest integer) in colored contours versus (Ra, Ch). The symbols correspond to each case's regime. Cases in the magnetocolumnar regime have $l_\perp/l_c \approx 1$, which is shown by the blue contour lines. The same holds for the magnetoplume regime, where the width of the plumes is also well predicted by linear theory. Based on Fig. 6, the following behavior holds: $l_\perp/l_c \approx 1$, allowing $l_\perp \sim \text{Ch}^{-1/6}H$ for the magnetocolumnar and magnetoplume regimes. Figure 6 also shows that $l_\perp/l_c$ begins to increase beyond 1 as plumes merge and increase in horizontal scale in the drifting plumes regime.

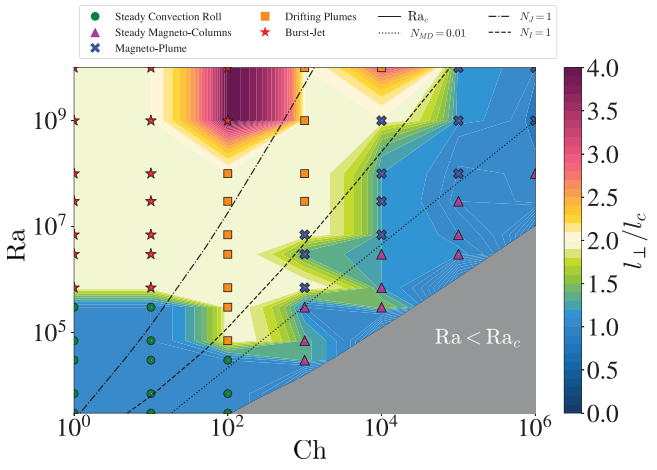

FIG. 6. Measured perpendicular length scale, $l_\perp$ normalized by the critical length scale predicted by magnetoconvection linear theory, l_c (using m_c to the nearest integer) against all values of Ra, Ch. The horizontal length scale is measured by inverting the peak wave number of the vertically and temporally averaged temperature fields.

Figure 7 shows measurements of the velocity, quantified by the time-averaged vertical and horizontal Reynolds number ($\langle\text{Re}_y\rangle_t$ and $\langle\text{Re}_x\rangle_t$, respectively) as a function of Ra, Ra_c for different values of Ch, denoted by various colors. The symbols correspond to each case's regime. Figure 7(a) shows the vertical velocity as a function of Ra. In the steady convection roll, steady magnetocolumns, and magnetoplumes regimes, $\langle\text{Re}_y\rangle_t$ grows with increasing Ra. However, for the drifting plumes and burst-jet regimes, the growth of $\langle\text{Re}_y\rangle_t$ with Ra slows, and for some cases there is a depression in $\langle\text{Re}_y\rangle_t$ with increasing Ra. This is due to the manifestation of strong zonal flows, which limit convective velocities in the vertical direction.

Figure 7(b) shows $\langle\text{Re}_x\rangle_t$ versus Ra, and a different trend is found. Each value of Ch has a slightly lower value of $\langle\text{Re}_x\rangle_t$ at a given Ra as increasing magnetic field suppresses flows perpendicular to the field. However, at a fixed value of Ch, $\langle\text{Re}_x\rangle_t$ grows monotonically with Ra.

We follow Sommeria and Moreau [58], Yan *et al.* [62] to find a scaling law for the velocity in the steady mag-

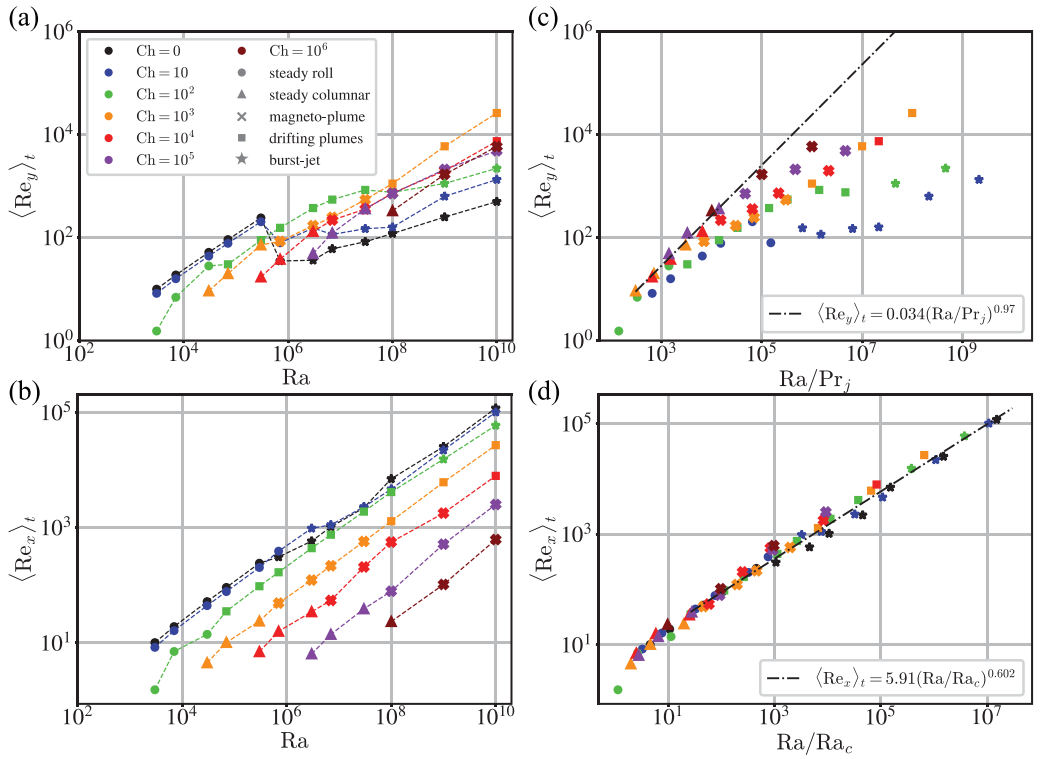

FIG. 7. Horizontal and vertical flow speeds. (a) Time-averaged horizontal Reynolds number, $\langle \mathrm{Re}_x \rangle_t$ versus the Rayleigh number. (b) $\langle \mathrm{Re}_x \rangle_t$ versus $\mathrm{Ra}/\mathrm{Ra}_c$, where the black dashed line gives the power-law fit of the data. (c) Time-averaged vertical Reynolds number, $\langle \mathrm{Re}_y \rangle_t$ versus the Rayleigh number. (d) $\langle \mathrm{Re}_y \rangle_t$ versus $\mathrm{Ra}/\mathrm{Pr}_j$, where the black dashed line gives the power-law fit of the data, and Pr_j is defined in Sec. IV A.

netocolumns regime, and suggest that the Joule dissipation acts as an "effective" viscosity. The Joule dissipation, when formulated as a viscous term that damps the flow speed, leads to a "Joule-Prandtl" number (Pr_j),

$$\mathrm{Pr}_j = \frac{\tau_\kappa}{\tau_j}, \tag{53}$$

where $\tau_\kappa = H^2/\kappa$ and τ_j is given by Eq. (47), where the parallel length scale has been scaled by H. Substituting these definitions for Pr_j gives

$$\mathrm{Pr}_j = \frac{\sigma B_0^2 H^2}{\rho \kappa}\left(\frac{l_\perp}{H}\right)^2. \tag{54}$$

Equation (54) can be simplified using $l_\perp \sim \mathrm{Ch}^{-1/6} H$, which holds for the steady magnetocolumns regime. This leads to

$$\mathrm{Pr}_j = \mathrm{Ch}^{2/3}\mathrm{Pr}. \tag{55}$$

Using Pr_j as the effective Prandtl number for this system yields a velocity scaling law relevant to a flow constrained by the imposed field is given by

$$\mathrm{Re} \sim \mathrm{Ra}/\mathrm{Pr}_j. \tag{56}$$

This is similar to a scaling law found by balancing the viscosity and buoyancy terms of Eq. (17), which yields $\mathrm{Re} \sim \mathrm{Ra}/\mathrm{Pr}$. In this case, the Joule dissipation, through the Lorentz force, acts like a viscosity damping the flow.

Figure 7(c) gives $\langle \mathrm{Re}_y \rangle_t$ versus $\mathrm{Ra}/\mathrm{Pr}_j$. We find a good collapse of the cases in the magnetocolumnar regime (denoted by triangles) using $\mathrm{Ra}/\mathrm{Pr}_j$. This agrees with Yan *et al.* [62], who by balancing the Lorentz force with buoyancy, also found $\mathrm{Re} \sim \mathrm{Ra}/\mathrm{Pr}_j$ for convection constrained by an imposed vertical magnetic field. This scaling, $\mathrm{Re} \sim \mathrm{Ra}/\mathrm{Pr}_j$, gives us a behavior that can be used in conjunction with the perpendicular length scale data for the steady magnetocolumns and magnetoplume regimes to construct an interaction parameter-based transition between these two regimes.

Figure 7(d) gives $\langle \mathrm{Re}_x \rangle_t$ against $\mathrm{Ra}/\mathrm{Ra}_c$. The ratio $\mathrm{Ra}/\mathrm{Ra}_c$ estimates the relative strength of buoyancy given a certain value of Ch. The following collapses the data well (for $\mathrm{Pr} = 1$),

$$\langle \mathrm{Re}_x \rangle_t = 5.39 \pm 1.17(\mathrm{Ra}/\mathrm{Ra}_c)^{0.61\pm0.01}. \tag{57}$$

This fit matches closely with Wang *et al.* [42], who carried out a study in a similar setup, namely 2D RBC with free-slip boundary conditions. Wang *et al.* [42] found $\mathrm{Re} \sim \mathrm{Ra}^{0.60}$ for jet-dominated flows (with fixed $\mathrm{Pr} = 10$). This scaling law for the velocity will be used for the drifting plumes and burst-jet regimes, where the horizontal velocity exceeds the vertical velocity.

V. INTERACTION PARAMETER-BASED TRANSITIONS

We use the trends found in our data along with the interaction parameter definitions given in Sec. III to construct three interaction parameter-based transition lines which can be used to predict where one regime transitions to the next in (Ra, Ch) space. Table I gives a summary of the five regimes, their main characteristics, and the length and velocity scalings that will be utilized here.

TABLE I. Summary of the five regimes and their characteristics. Each column gives the regime name, the ratio of horizontal to vertical velocities, the variance of the vertical velocity, the value of τ_j (the average time spent in the jet phase), and the scaling laws used for the perpendicular length scale and velocity ($l_\perp$, Re) when building interaction parameter transition lines between the regimes as discussed in Sec. V.

Regime name	Horizontal to vertical velocity ratio	var(Re_y)	τ_j	$l_\perp \sim$	Re $\sim$
Steady convection roll	$\langle \mathrm{Re}_x\rangle_t \approx \langle \mathrm{Re}_y\rangle_t$	0	0	1	
Steady magnetocolumns	$\langle \mathrm{Re}_x\rangle_t \leqslant \langle \mathrm{Re}_y\rangle_t$	0	0	$\mathrm{Ch}^{-1/6}$	$\mathrm{Ra}/\mathrm{Pr}_j$
Magnetoplumes	$\langle \mathrm{Re}_x\rangle_t \leqslant \langle \mathrm{Re}_y\rangle_t$	>0	0	$\mathrm{Ch}^{-1/6}$	
Drifting plumes	$\langle \mathrm{Re}_x\rangle_t > \langle \mathrm{Re}_y\rangle_t$	>0	0		$(\mathrm{Ra}/\mathrm{Ra}_c)^{3/5}$
Burst-jet	$\langle \mathrm{Re}_x\rangle_t > \langle \mathrm{Re}_y\rangle_t$	>0	>0	$\Gamma = 2$	$(\mathrm{Ra}/\mathrm{Ra}_c)^{3/5}$

The first transition line separates the steady magnetocolumns regime from the magnetoplumes regime, which are both "magnetically dominated" flows in which gradients parallel to the applied field are limited. In both regimes, the data revealed $l_\perp \sim \mathrm{Ch}^{-1/6}H$. To find where the magnetoplumes regime transitions to the steady magnetocolumns regime, we note that only in the latter, inertial effects are neglected to yield the velocity scale $\mathrm{Re} \sim \mathrm{Ra}/\mathrm{Pr}_j$. The magnetoplumes regime then transitions to the steady magnetocolumns regime along an interaction parameter line given by Eq. (48) using $\mathrm{Re} \sim \mathrm{Ra}/\mathrm{Pr}_j$, in addition to $l_\perp \sim \mathrm{Ch}^{-1/6}H$. This substitution yields

$$N_{\mathrm{MD}} = \frac{\mathrm{Ch}}{\mathrm{Re}}\left(\frac{l_\perp}{H}\right)^3 \sim \frac{\mathrm{Ch}^{7/6}\mathrm{Pr}}{\mathrm{Ra}}. \tag{58}$$

The second transition is between the two "intermediate" regimes (magnetoplumes and drifting plumes) rather than the end-member flows (steady magnetocolumns and burst-jet). In the magnetoplumes regime, the structures have a perpendicular length scale that, as previously stated follows $l_\perp \sim \mathrm{Ch}^{-1/6}H$. The distinguishing characteristic between the these two regimes is that the horizontal velocity dominates the vertical velocity in the drifting plumes regime, as defined in Sec. IV. Therefore, the crossover to the drifting plumes regime from the magnetoplumes regime will occur once the velocity follows $\mathrm{Re} \sim (\mathrm{Ra}/\mathrm{Ra}_c)^{0.61} \approx (\mathrm{Ra}/\mathrm{Ra}_c)^{3/5}$ as found in Sec. IV A. Using Eq. (48)

$$N_I = \frac{\mathrm{Ch}}{\mathrm{Re}}\left(\frac{l_\perp}{H}\right)^3 \sim \frac{\mathrm{Ch}^{1/2}\mathrm{Pr}}{(\mathrm{Ra}/\mathrm{Ra}_c)^{3/5}}. \tag{59}$$

The final transition is between the drifting plumes regime and burst-jet regime, which is characterized by strong, domain-filling zonal flows, or jets (J). In such flows, $l_\perp/H \sim \Gamma = 2$, though the velocity scale continues to follow $\mathrm{Re} \sim (\mathrm{Ra}/\mathrm{Ra}_c)^{3/5}$. For this transition line, Eq. (51) is used, since the system is not constrained by the magnetic field and strong vertical shears exist in the flow. The transition to the jet regime is

$$N_J = \frac{\mathrm{Ch}}{\mathrm{Re}}\left(\frac{l_\perp}{H}\right) \sim \frac{2\ \mathrm{Ch}\ \mathrm{Pr}}{(\mathrm{Ra}/\mathrm{Ra}_c)^{3/5}}. \tag{60}$$

Figure 8(a) gives N_{MD} against var(Re_y) for cases only in these two regimes, where values greater than zero are used to separate the steady magnetocolumns to the magnetoplume regime. This transition occurs at $N_{\mathrm{MD}} \approx 0.01$. Figure 8(b) shows N_I against $\langle \mathrm{Re}_x\rangle_t/\langle \mathrm{Re}_y\rangle_t$, the ratio that separates the two intermediate regimes (the magnetoplume and the drifting plumes) from one another with a transition occurring at $N_I \approx 1$. Figure 8(c) shows N_J against τ_{jet}, where values greater than zero are used to parse the drifting plumes to the burst-jet regime. There is a reasonable collapse of the data at $N_J \approx 0.1$–1.

Figure 9 outlines the values of (Ra, Ch) over which we have run simulations. The colors and symbols corre-

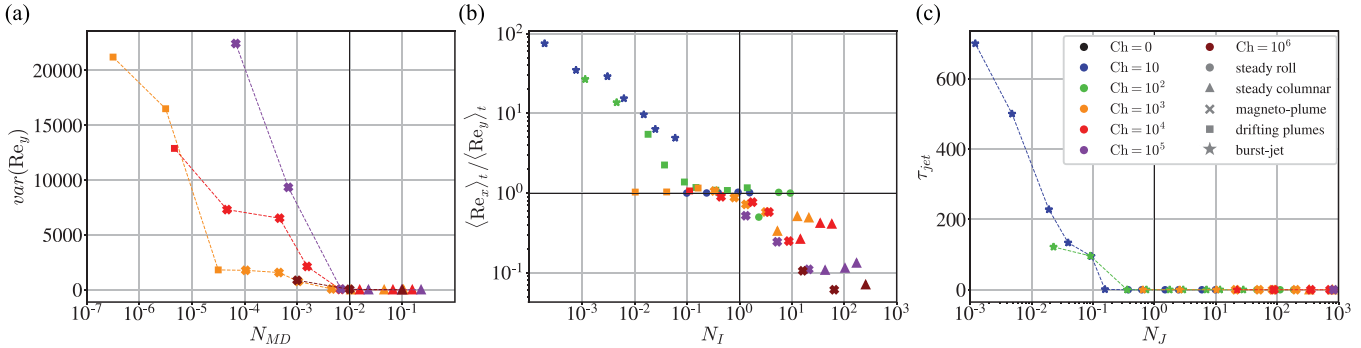

FIG. 8. Shows how the scaling laws derived in Sec. III collapse the quantities used to separate the regimes. (a) The variance of Re_y, which characterizes unsteadiness, against the scaling law derived for the transition from the magnetocolumnar to the magnetoplume regime, N_{MC}. Only cases in these two regimes are shown for clarity. (b) The ratio of the horizontal and vertical velocities $\langle \mathrm{Re}_x\rangle_t$ and $\langle \mathrm{Re}_y\rangle_t$, used to distinguish between the magnetoplumes and drifting plumes regime, against the scaling law derived for N_{MP}. (c) The measured value of τ_{jet}, where values greater than 0 are reserved for the burst-jet regime, against the scaling law derived for N_j.

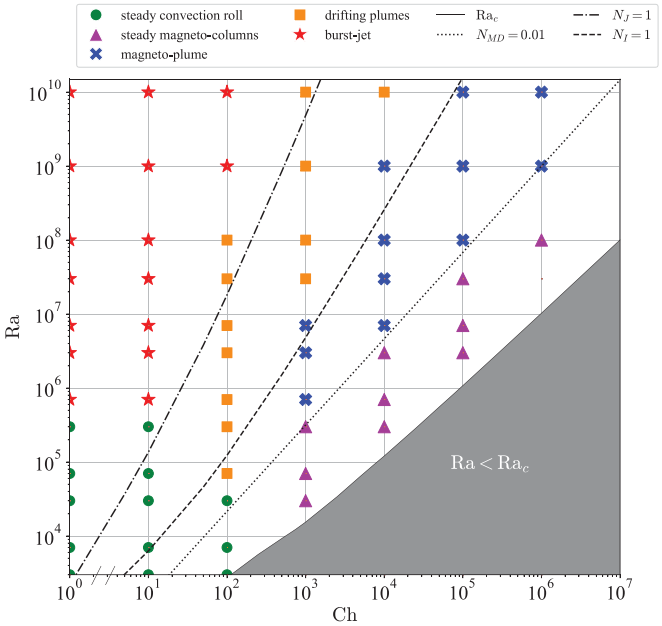

FIG. 9. The Rayleigh and Chandrasekhar number ranges (at fixed aspect ratio and Prandtl number) over which we have found steady convection rolls (green circles), steady magnetocolumns (purple triangles), unsteady to turbulent magnetoplumes (blue crosses), drifting magnetoplumes (orange squares), or jets with intermittent turbulent convective bursts (red stars). The solid black line indicates the critical Rayleigh number, and the dotted, dashed, and dash-dot lines give the interaction parameter transitions between the regimes, discussed further in Sec. III.

spond to regime classifications and the three lines (dotted, dashed, dash-dot) give approximate regime transitions, based on Eqs. (58), (59), and (60). These transition lines provide adequate estimates for where regime transitions occur in our data.

A. Dependence on the Prandtl number

The interaction parameter-based transition line given by Eq. (60) will be used in Sec. VI to predict the truncation depth of Jupiter's large-scale jets. We test this transition line further by varying Pr, which may be relevant to Jupiter where $\mathrm{Pr}\approx 0.1$ [35]. Four additional cases are run at fixed $\mathrm{Ra}=7\times10^6$, $\mathrm{Ch}=10^2$, $\Gamma=2$ where $\mathrm{Pr}\in\{0.1,0.3,3,10\}$. Details of the cases, including the value of N_J, are given in Table II. Over this range, $0.177\leqslant N_J\leqslant 17.71$. In all four cases, the flows are unsteady and $\langle \mathrm{Re}_x\rangle_t > \langle \mathrm{Re}_y\rangle_t$. However, at $\mathrm{Pr}=0.1$, 0.3, the average time spent in the jet phase is larger than zero with values $t_{\mathrm{jet}}=98.57,\ 12.39$, respectively. We then follow the definitions detailed in Table I to classify each case into a regime. Figure 10(a) shows N_J as a function of Pr where the markers denote which case the regime is in. The transition between the burst-jet and drifting plumes regime occurs at $N_J\approx 1$, consistent with the transition observed in Fig. 9 for $\mathrm{Pr}=1$ and over a range of Ch, Ra.

TABLE II. Details of the DNS for fixed $\mathrm{Ra}=7\times10^6$ and $\mathrm{Ch}=10^2$ as we vary Pr. Each row gives Pr, N_J according to Eq. (60), vertical resolution n_y, horizontal resolution n_x, the time average of the Nusselt number ($\langle \mathrm{Nu}\rangle_t$), and the area-time averages of the horizontal Reynolds number and vertical Reynolds number ($\langle \mathrm{Re}_x\rangle_t$, $\langle \mathrm{Re}_y\rangle_t$), respectively.

Pr	N_J	n_y	n_x	$\langle \mathrm{Nu}\rangle_t$	$\langle \mathrm{Re}_x\rangle_t$	$\langle \mathrm{Re}_y\rangle_t$
0.1	0.177	360	720	11.37	6406.65	1910.06
0.3	0.531	360	720	15.50	2305.52	895.99
1	1.77	168	452	23.35	754.72	546.60
3	5.31	360	720	26.51	237.67	220.48
10	17.7	360	720	24.28	60.61	57.00

VI. GEOPHYSICAL IMPLICATIONS

We have conducted a systematic survey of quasistatic magnetoconvection in a quasi-2D, horizontally periodic Cartesian geometry with stress-free velocity and fixed temperature boundary conditions. Five primary flow regimes are found: (i) steady convection rolls, (ii) steady magnetocolumns, (iii) unsteady to turbulent magnetoplumes, (iv) horizontally drifting plumes, and (v) jets with intermittent turbulent convective bursts. The regimes have unique length scale, momentum transfer, and time-dependence characteristics. regime transition lines are derived based on interaction parameter theory. The regime transition relevant to the magnetic damping of Jovian jet flows is that between the drifting plumes to burst-jet regimes. This occurs at a jet-based interaction parameter of $N_J\approx 1$. We now seek to find the depth at which the Jovian interaction parameter crosses this threshold in the semiconducting region of Jupiter.

The quasi-steady azimuthal component of the vorticity equation in cylindrical coordinates $(\hat{\boldsymbol{s}},\hat{\boldsymbol{z}},\hat{\boldsymbol{\phi}})$ controlling the dynamics in the bulk of Jupiter's outer molecular envelope is [93–95]

$$\left([\boldsymbol{u}\cdot\boldsymbol{\nabla}\boldsymbol{\omega}]_\phi+2\Omega\frac{\partial u_\phi}{\partial z}\right)\simeq\alpha g\frac{\partial T}{\partial s}, \tag{61}$$

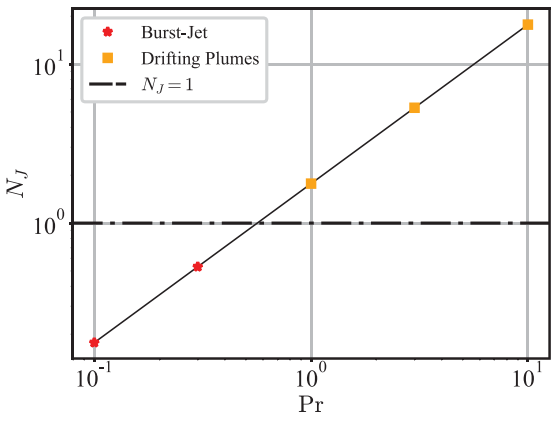

FIG. 10. The interaction parameter-based transition line, Eq. (60), tested by varying Pr while $\mathrm{Ra}=7\times10^6$, $\mathrm{Ch}=10^2$. The markers correspond to the case's regime and the horizontal dash-dot line demarcates where $N_J\approx 1$.

where we have simplistically adopted the Boussinesq approximation to treat the density [96,97]. Equation (61), neglecting the first term on the left-hand side, is known as thermal wind balance [98–100]. The left-hand side of Eq. (61) are the inertial terms in the system, where the first represents advection and the second represents vortex stretching. We can take the ratio of these terms to one another, which gives

$$\frac{[\boldsymbol{u}\cdot\nabla\boldsymbol{\omega}]_\phi}{2\Omega\frac{\partial u_\phi}{\partial z}} \sim \frac{U}{2\Omega\mathcal{L}} = \mathrm{Ro}, \tag{62}$$

where Ro is known as the Rossby number, $\mathcal{L}$ is a characteristic length scale, U is a characteristic velocity scale, and Ω is the planetary rotation rate. We can estimate Ro for Jupiter's molecular envelope jets using a typical jet velocity of $U = 50$ m/s, a large-scale jet width of $\mathcal{L} = 10^4$ km, and planetary rotation rate of $\Omega = 1.74\times10^{-4}$ 1/s, which gives [101]

$$\mathrm{Ro} = \frac{U}{2\Omega\mathcal{L}} \sim 0.01 \ll 1. \tag{63}$$

Furthermore, strong convective turbulence could homogenize the large-scale temperature anomalies such that $\partial T/\partial s$ is small. For the low Rossby jets, this implies that the velocity field may vary weakly along the axial coordinate such that $\partial u_\phi/\partial z$ in Eq. (61) is also small [102].

Jupiter's electrical conductivity increases with radius, possibly leading to a larger Lorentz force at the base of the jets compared to the molecular envelope. Then, the hydrodynamic thermal wind balance is replaced by the thermomagnetic wind balance [103]

$$\left([\boldsymbol{u}\cdot\nabla\boldsymbol{\omega}]_\phi + 2\Omega\frac{\partial u_\phi}{\partial z}\right) \simeq \alpha g\frac{\partial T}{\partial s} + \frac{1}{\rho_0}[\nabla\times(\boldsymbol{J}\times\boldsymbol{B})]_\phi. \tag{64}$$

In the limit of strong thermal mixing, this simplifies to

$$\left([\boldsymbol{u}\cdot\nabla\boldsymbol{\omega}]_\phi + 2\Omega\frac{\partial u_\phi}{\partial z}\right) \approx \frac{1}{\rho_0}[\nabla\times(\boldsymbol{J}\times\boldsymbol{B})]_\phi. \tag{65}$$

Further, by assuming $Rm \leqslant 1$ at the base of the jets [16], we can use $\boldsymbol{J} = \sigma(\boldsymbol{u}\times\boldsymbol{B})$ to recast this expression as

$$\left([\boldsymbol{u}\cdot\nabla\boldsymbol{\omega}]_\phi + 2\Omega\frac{\partial u_\phi}{\partial z}\right) \simeq \frac{1}{\rho_0}[\nabla\times(\sigma\boldsymbol{u}\times\boldsymbol{B}\times\boldsymbol{B})]_\phi. \tag{66}$$

The right-hand side of Eq. (66) can be simplified by allowing $\boldsymbol{u} = \boldsymbol{u}_\perp + \boldsymbol{u}_\parallel$, where $\perp, \parallel$ denote directions relative to the magnetic field $\boldsymbol{B}$. It becomes

$$\left([\boldsymbol{u}\cdot\nabla\boldsymbol{\omega}]_\phi + 2\Omega\frac{\partial u_\phi}{\partial z}\right) \simeq \frac{-|B|^2|}{\rho_0}[\sigma(\nabla\times\boldsymbol{u}_\perp) + (\nabla\sigma)\times\boldsymbol{u}_\perp]_\phi. \tag{67}$$

We reduce Eq. (67) further by allowing $\boldsymbol{u}_\perp = u_s\hat{\boldsymbol{s}} + u_\phi\hat{\boldsymbol{\phi}} + u_z\hat{\boldsymbol{z}}$. Noting that velocity field varies weakly along the axial coordinate for low Rossby flows, and σ only varies in radius gives

$$\left([\boldsymbol{u}\cdot\nabla\boldsymbol{\omega}]_\phi + 2\Omega\frac{\partial u_\phi}{\partial z}\right) \simeq \frac{-|B|^2|}{\rho_0}\left[\sigma\left(\frac{\partial u_z}{\partial s}\right) + \left(u_z\frac{\partial\sigma}{\partial s}\right)\right]. \tag{68}$$

We can scale both terms on the right-hand side of Eq. (68), and from left to right they are

$$\frac{B_0^2\sigma u_z}{\rho_0\mathcal{L}_{\mathrm{jet}}}, \quad \frac{B_0^2\sigma u_z}{\rho_0\mathcal{L}_\sigma}, \tag{69}$$

where B_0 is a characteristic magnetic field strength in the semiconducting region, u_z is a characteristic meridional velocity scale, $\mathcal{L}_{\mathrm{jet}}$ is a characteristic jet scale, and

$$\mathcal{L}_\sigma = \frac{1}{\sigma}\left|\frac{\partial\sigma}{\partial s}\right|^{-1} \tag{70}$$

is an electrical conductivity scale height. This can be calculated using the results of French *et al.* [17] and Jones [105]. The terms in Eq. (69) only differ by the length scales in their denominators. Comparing the characteristic values $\mathcal{L}_\sigma \approx$ 350 km and $\mathcal{L}_{\mathrm{jet}} \approx 10\,000$ km we find

$$\mathcal{L}_\sigma \ll \mathcal{L}_{\mathrm{jet}}. \tag{71}$$

The second term on the right-hand side of Eq. (68), controlled by the planet's radially increasing electrical conductivity, is the largest term, and we are left with

$$\left([\boldsymbol{u}\cdot\nabla\boldsymbol{\omega}]_\phi + 2\Omega\frac{\partial u_\phi}{\partial z}\right) \simeq \frac{|B|^2}{\rho_0}\left(u_z\frac{\partial\sigma}{\partial s}\right). \tag{72}$$

We can balance the two inertial terms with the Lorentz term in Eq. (72) to construct two interaction parameter functions. For the first, we take the ratio of the Lorentz to the advection term in Eq. (66) and note that $\omega_\phi \sim u_z/\mathcal{L}_{\mathrm{jet}}$ to arrive at an interaction parameter

$$N = \frac{B_0^2\sigma(\tilde{r})\mathcal{L}_{\mathrm{jet}}^2}{u_\phi(\tilde{r})\rho_0\,\mathcal{L}_\sigma}, \tag{73}$$

where $\tilde{r} = r/r_j$ is radial position normalized by Jupiter radius $r_j = 69,894$ km, ρ_0 is the mean density averaged over $0.90 < \tilde{r} < 1.0$, and $\sigma(\tilde{r})$ is the electrical conductivity as a function of nondimensional radial position.

For the second interaction parameter, we take the ratio of the Lorentz to the Coriolis term in Eq. (72), which gives a Coriolis-based interaction parameter (also known as the Elsasser number, Λ) [56,106–109]:

$$N_\Omega = \Lambda = \frac{B_0^2\sigma(\tilde{r})}{2\rho_0\,\Omega}\left(\frac{u_z}{u_\phi}\right)\left(\frac{\mathcal{L}_{\mathrm{jet}}}{\mathcal{L}_\sigma}\right). \tag{74}$$

Though our simple model differs greatly from the fully 3D, anelastic, spherical Jovian system, based on Eq. (61) the low Rossby jets may extend into the molecular interior with little variation in the direction of the axis of rotation. Thus, we choose to extrapolate the transitions found in our 2D model, and naively assume that magnetodamping may slow the jets when the Lorentz force is greater than inertia, or the depth at which N and N_Ω exceed 1.

To calculate the local values of N and N_Ω, values for $\sigma(\tilde{r})$, ρ_0, and $\mathcal{L}_\sigma$ are found by employing the results of French *et al.* [17] and Jones [105]. The density is averaged over $0.90 < \tilde{r} < 1.0$, which gives $\rho_0 = 267$ kg/m^3. To estimate B_0 in the semiconducting region, the Juno surface field model is extrapolated to 3000 km in depth [110] and averaged

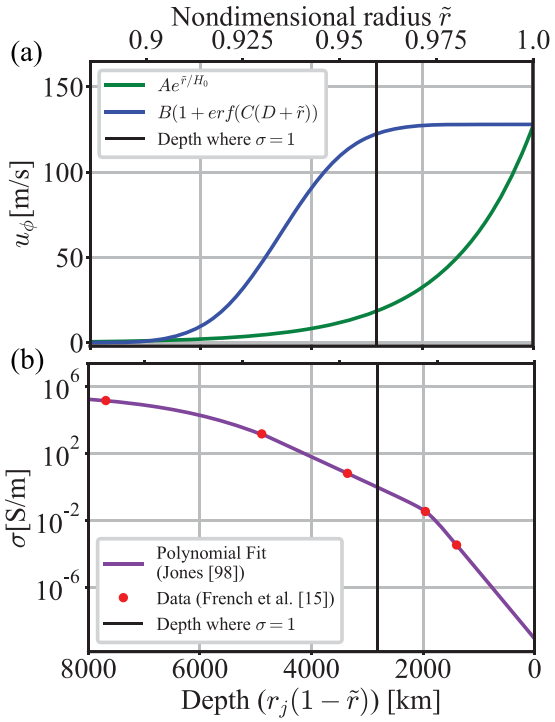

FIG. 11. (a) Estimated zonal flow decay with nondimensional radius (top axis) or depth from the surface (bottom axis) for two functions. Green is based on Kaspi *et al.* [104], with $u_\phi(\tilde{r}) = Ae^{\tilde{r}/H_0}$ and A a constant to fix the cloud level zonal-flow magnitude to 125 m/s. Blue is an error function which yields a cloud level zonal-flow magnitude of 125 m/s and decays sharply once $\sigma = 1$ demarcated by a black line. (b) Electrical conductivity with nondimensional radius (top axis) or depth from the surface (bottom axis). The red points show data from French *et al.* [17] and the purple line shows the polynomial fit to these points carried out by Jones [105]. The black line gives the depth at which $\sigma = 1$.

at 50 degrees latitude, which gives ≈7.92 Gauss. The velocity scale $u_z \approx 1$ m/s is found using zonal-mean meridional velocity data from Cassini spacecraft observations [111,112].

We use two different functions for the zonal velocity, $u_\phi(\tilde{r})$. For the first, we employ the exponential decay model from Kaspi *et al.* [104] derived using anelastic thermal wind balance

$$u_\phi(\tilde{r}) = Ae^{\tilde{r}/H_0}, \tag{75}$$

where A is a constant fixed to yield a sensible cloud-level zonal flow of 125 m/s [14], and $H_0 = H/r_j$ is the e-folding depth. According to Kaspi *et al.* [104], the e-folding depth that yields a best fit to the Juno odd gravity harmonic data is $H = 1471$ km. The green curve in Fig. 11(a) gives this constructed zonal flow profile in the semiconducting region from $\tilde{r}$ ranging from about 0.90 (8000 km in depth) to 1.0.

However, the exact shape of the zonal flow decay remains ambiguous [100]. We construct an additional zonal flow profile where $u_{\text{zonal}}(\tilde{r})$ only decays after the planet's electrical conductivity exceeds 1 S/m. The profile meets the criteria that in the highly conducting region of Jupiter with electrical conductivity greater than 1000 S/m, the zonal flow is likely

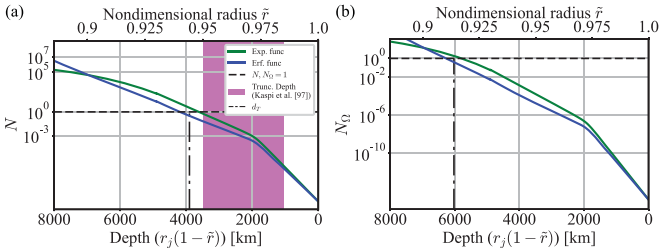

FIG. 12. (a) Value of N based on Eq. (73) with nondimensional radius (top axis) and depth from the surface (bottom axis). The green and blue lines correspond to the exponential and error functions, respectively. The purple box indicates the range of truncation depths from the Juno mission Kaspi *et al.* [104]. (b) Value N_Ω given by Eq. (74). In both panels, the black dashed line indicates where the interaction parameter crosses 1, and the black dash-dot line corresponds to the truncation depth, d_T.

on the order of 1 cm/s or less [19,113,114] and is defined by

$$u_\phi(\tilde{r}) = B\,\{1 + \text{erf}[C(D+\tilde{r})]\}, \tag{76}$$

where $B = 64.0$, $C = 49.1$, and $D = -0.946$ yield a cloud-level zonal flow on the order of 125 m/s. The blue curve in Fig. 11(a) shows this profile. Figure 11(b) shows Jupiter's estimated electrical conductivity with radius, and we mark the depth at which $\sigma = 1$ with a solid black line.

Figure 12(a) gives N against nondimensional radius (top axis) and depth from the surface (bottom axis) using these approximations. A value of $N = 1$ (black dashed line) corresponds to a depth at which the jet truncation process may commence at about $d_T = 3600$, 4200 km for the exponential and error velocity functions respectively (black dash dot line, the average between the two is shown).

Figure 12(b) gives N_Ω against nondimensional radius (top axis) and depth from the surface (bottom axis). A value of $N_\Omega = 1$ (black dashed line) is not reached until a depth of about $d_T = 6000$, 6300 km for the exponential and error functions respectively. Recent studies based on Juno measurements of the odd gravity harmonics have constrained the zonal flow depth to about 3000 km [104,115].

Extrapolating our 2D results suggests that Lorentz force likely cannot solely brake the jets on Jupiter, and additional mechanisms are needed to fully truncate them [19,33,46]. For instance, Christensen *et al.* [103] carried out axisymmetric shell models that included both electromagnetic drag and a stably stratified layer extending upward into the region of low electrical conductivity, which may exist on the Gas Giants [98,116,117]. They found that without this stable layer, the Lorentz force could not truncate the jets. Thus, the exact braking process of Jovian jets remains an open question.

ACKNOWLEDGMENTS

We gratefully acknowledge the NSF Geophysics Program (EAR Awards No. 1620649 and No. 1853196). We also thank Y. Xu and J. Abbate for their useful discussions. Computing time on TACC's Stampede2 was provided care of XSEDE Award No. PHY21005.

TABLE III. Details of the DNS for Ch $= 0, 10, 10^2, 10^3$ where Pr $= 1, \Gamma = 2$. Each row gives Ch, Ra, its ratio above onset $\mathrm{Ra}/\mathrm{Ra}_c$, vertical resolution n_y, horizontal resolution n_x, the time average of the Nusselt number ($\langle \mathrm{Nu} \rangle_t$), and the time averages of the horizontal Reynolds number and vertical Reynolds number ($\langle \mathrm{Re}_x \rangle_t$, $\langle \mathrm{Re}_y \rangle_t$), respectively.

Ch	Ra	$\mathrm{Ra}/\mathrm{Ra}_c$	n_y	n_x	$\langle \mathrm{Nu} \rangle_t$	$\langle \mathrm{Re}_x \rangle_t$	$\langle \mathrm{Re}_y \rangle_t$
0	3×10^3	4.56	96	356	3.08	10.14	9.99
0	7×10^3	10.64	96	356	4.34	19.23	18.86
0	3×10^4	45.62	96	356	7.57	52.19	51.87
0	7×10^4	1.06×10^2	96	356	10.32	91.94	91.71
0	3×10^5	4.56×10^2	120	380	17.31	241.76	241.62
0	7×10^5	1.06×10^3	120	380	4.33	309.68	35.28
0	3×10^6	4.56×10^3	132	404	3.46	584.80	36.38
0	7×10^6	1.06×10^4	132	404	3.58	1030.43	60.53
0	3×10^7	4.56×10^4	168	452	4.03	2214.02	83.24
0	1×10^8	1.52×10^5	516	1032	4.73	7030	120.1
0	1×10^9	1.52×10^6	1024	2048	6.85	25240	251.1
0	1×10^{10}	1.52×10^7	3072	6144	8.61	118270	500.20
10	3×10^3	3.25	96	356	2.78	8.39	8.29
10	7×10^3	7.58	96	356	3.99	16.34	15.94
10	3×10^4	32.5	96	356	7.04	44.42	43.96
10	7×10^4	75.8	96	356	9.66	77.88	77.59
10	3×10^5	3.25×10^2	120	380	16.30	203.76	203.61
10	7×10^5	7.58×10^2	120	380	9.64	390.77	79.37
10	3×10^6	3.25×10^3	132	404	13.78	973.89	153.56
10	7×10^6	7.58×10^3	132	404	8.99	1115.95	115.44
10	3×10^7	3.25×10^4	168	452	9.06	2295.66	148.98
10	1×10^8	1.08×10^5	360	720	9.14	4656.67	159.79
10	1×10^9	1.08×10^6	1536	3072	22.3	23497	2200.4
10	1×10^{10}	1.08×10^7	2048	4096	41.2	101131	1347
10^2	3×10^3	1.13	96	356	1.17	1.54	1.54
10^2	7×10^3	2.64	96	356	2.55	7.11	6.96
10^2	3×10^4	11.3	96	356	4.703	14.10	28.22
10^2	7×10^4	26.4	96	356	5.61	35.41	30.35
10^2	3×10^5	1.13×10^2	120	380	10.30	96.46	89.38
10^2	7×10^5	2.64×10^2	120	380	13.48	168.51	154.96
10^2	3×10^6	1.13×10^3	132	404	19.94	441.64	375.33
10^2	7×10^6	2.64×10^3	168	452	23.35	754.73	547.60
10^2	3×10^7	1.13×10^4	192	500	28.97	1900.81	843.33
10^2	1×10^8	3.77×10^4	256	636	32.88	4149.99	758.15
10^2	1×10^9	3.77×10^5	768	1536	43.06	15246	1123.95
10^2	1×10^{10}	3.77×10^6	3072	6144	61.05	59423	2214.6
10^3	3×10^4	1.97	96	356	2.35	4.52	9.23
10^3	7×10^4	4.60	96	356	3.96	10.18	19.99
10^3	3×10^5	19.7	120	380	7.48	23.94	71.96
10^3	7×10^5	46.0	120	380	9.28	49.11	84.79
10^3	3×10^6	1.97×10^2	132	404	13.25	123.31	171.07
10^3	7×10^6	4.60×10^2	168	452	16.23	218.0	247.99
10^3	3×10^7	1.97×10^3	168	452	24.56	576.78	543.45
10^3	1×10^8	6.58×10^3	252	636	36.25	1294.93	1199.18
10^3	1×10^9	6.58×10^4	984	1964	79.403	6136.48	5936.12
10^3	1×10^{10}	6.58×10^5	1536	3072	165.22	27012	26218

APPENDIX A: DATA TABLES

In this study, we conducted a survey of quasistatic magnetoconvection in a quasi-2D, horizontally periodic Cartesian geometry which stress-free velocity and fixed temperature boundary conditions. For a majority of the cases, we fixed the aspect ratio to $\Gamma = 2$. The details of the DNS are provided in Tables III and IV.

APPENDIX B: BENCHMARKING THE CODES

A set of Ch $= 0$ cases for this study (TS) and Dedalus (D) were benchmarked to [37] (G). The time-averaged Nusselt number, $\langle \mathrm{Nu} \rangle_t$ was calculated for seven different Rayleigh numbers at $\Gamma = 2$, Pr $= 1$. In addition, this study and Dedalus were benchmarked to one another for a set of eight different Ch $\neq 0$ with varying Ra. Differences in the three codes yield

TABLE IV. Details of the DNS for Ch $= 10^4, 10^5, 10^6$ where Pr $= 1$, $\Gamma = 2$. Each row gives Ch, Ra, its ratio above onset Ra/Ra$_c$, vertical resolution n_y, horizontal resolution n_x, the time average of the Nusselt number ($\langle \mathrm{Nu} \rangle_t$), and the area-time averages of the horizontal Reynolds number and vertical Reynolds number ($\langle \mathrm{Re}_x \rangle_t$, $\langle \mathrm{Re}_y \rangle_t$), respectively.

Ch	Ra	Ra/Ra$_c$	n_y	n_x	$\langle \mathrm{Nu} \rangle_t$	$\langle \mathrm{Re}_x \rangle_t$	$\langle \mathrm{Re}_y \rangle_t$
10^4	3×10^5	2.50	120	380	3.17	5.47	23.17
10^4	7×10^5	5.84	120	380	5.78	12.33	50.96
10^4	3×10^6	25.0	132	404	10.30	34.72	131.55
10^4	7×10^6	58.4	192	380	14.48	58.97	205.67
10^4	3×10^7	2.50×10^2	192	452	23.61	167.38	471.86
10^4	1×10^8	8.34×10^2	216	472	31.09	384.21	775.10
10^4	1×10^9	8.34×10^3	576	1172	59.03	1786.98	1988.51
10^4	1×10^{10}	8.34×10^4	1536	3072	112.7	7924.37	7441.40
10^5	3×10^6	2.78	132	404	4.04	6.45	48.73
10^5	7×10^6	6.49	168	452	8.42	14.06	122.81
10^5	3×10^7	27.8	168	452	16.38	39.03	362.61
10^5	1×10^8	92.73	192	500	26.01	78.90	714.50
10^5	1×10^9	9.27×10^2	360	692	58.89	516.79	2112.05
10^5	1×10^{10}	9.27×10^3	1536	3072	115.50	2520.92	4850.22
10^6	1×10^8	9.72	96	356	14.47	23.49	332.0
10^6	1×10^9	97.2	384	764	38.36	103.37	1689.52
10^6	1×10^{10}	9.72×10^3	1536	3072	108.34	621.39	5870.90

errors less than 0.15%. Both this study and Dedalus converged to the values listed in the table as the resolution was increased and the simulations were run for longer periods of time. Table V gives the results.

APPENDIX C: HEAT TRANSFER DISCUSSION

Each regime has distinct heat transport behaviors. The time variation of these characteristics was given in Sec. IV. Here, we carry out a more comprehensive discussion of how $\langle \mathrm{Nu} \rangle_t$ varies with Ra and Ra/Ra$_c$. Similar analysis of heat transfer is done in many studies of convection, rotating convection, and magnetoconvection [7,9,37,62,78–82].

TABLE V. Comparison of the time-averaged Nusselt number for this study (TS), Dedalus (D), and Goluskin *et al.* [37] (G). Each row gives the set of input parameters, and the time-averaged Nusselt number from each code.

Γ	Ra	Ch	$\langle \mathrm{Nu} \rangle_t(TS)$	$\langle \mathrm{Nu} \rangle_t(D)$	$\langle \mathrm{Nu} \rangle_t(G)$.
2	10^4	0	4.988	4.988	4.993
2	1.75×10^4	0	6.184	6.183	6.188
2	2×10^4	0	6.505	6.505	6.509
2	10^5	0	11.740	11.736	11.738
2	5×10^5	0	3.553	0	3.530
2	10^6	0	3.710	0	3.714
2	2.5×10^6	0	3.584	0	3.540
2	3×10^5	10	16.300	16.299	–
2	3×10^5	10^2	10.293	10.297	–
2	3×10^5	10^4	3.170	3.173	–
2	1×10^8	10^6	14.486	14.478	–
2	3×10^6	10	13.169	13.779	–
2	3×10^7	10^2	29.025	28.973	–
2	3×10^6	10^3	13.234	13.250	–
2	1×10^8	10^5	25.983	26.012	–

Figure 13(a) gives $\langle \mathrm{Nu} \rangle_t$ versus Ra. In the steady convection roll, steady magnetocolumns, and magnetoplumes regimes, $\langle \mathrm{Nu} \rangle_t$ grows as Ra is increased. However, in the

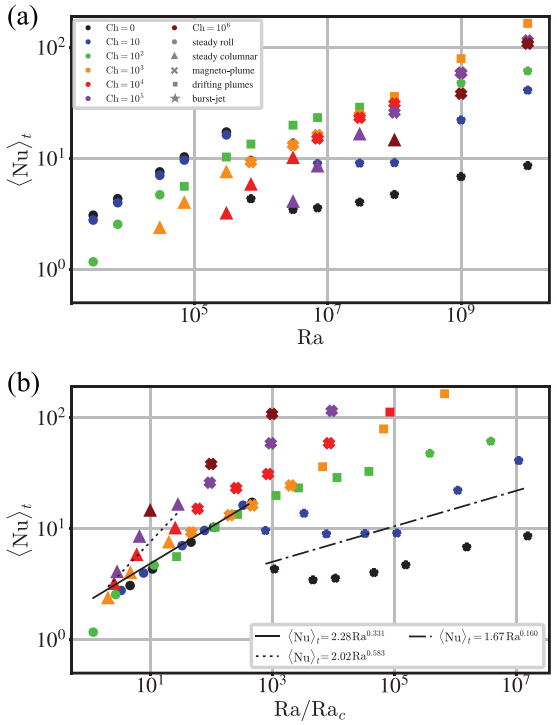

FIG. 13. Time-averaged heat transfer. (a) Time-averaged Nusselt number, $\langle \mathrm{Nu} \rangle_t$, versus the Rayleigh number. (b) $\langle \mathrm{Nu} \rangle_t$ versus Ra/Ra$_c$. Each line gives a power law fit of the data for the five different regimes. The solid black line gives the steady convection rolls regime, dotted line gives the steady magnetocolumns regime and dash-dot line gives the burst-jet regime. Power law fits for the magnetoplumes and drifting plumes regimes are similar to the steady convection rolls regime and are not displayed in the figure.

drifting plumes and burst-jet regimes, the growth of $\langle \mathrm{Nu} \rangle_t$ with Ra slows, and for some cases there is a depression in $\langle \mathrm{Nu} \rangle_t$ with increasing Ra. The zonal flows in these cases limit convective velocities and thus heat transport across the layer.

Figure 13(b) gives $\langle \mathrm{Nu} \rangle_t$ versus $\mathrm{Ra}/\mathrm{Ra}_c$. We provide a power law fit to the cases in each regime. In the steady convection roll regime, the power law fit yields $\mathrm{Nu} \sim (\mathrm{Ra}/\mathrm{Ra}_c)^{0.331}$ (black solid line), which is similar to the behavior found in Goluskin *et al.* [37]. Similar laws are found in the magnetoplumes [$\mathrm{Nu} \sim (\mathrm{Ra}/\mathrm{Ra}_c)^{0.327}$] and drifting plumes [$\mathrm{Nu} \sim (\mathrm{Ra}/\mathrm{Ra}_c)^{0.319}$] regimes, likely due to the ability for the convective plumes in both regimes to transfer heat efficiently across the layer. In the latter, the coefficient is slightly lower than the scaling found in the steady convection roll regime due to the manifestation of relatively weak zonal flows. The steepest fit comes from the magnetocolumns regime where $\mathrm{Nu} \sim (\mathrm{Ra}/\mathrm{Ra}_c)^{0.583}$ (dotted line). The columnar flows are able to efficiently transfer heat as it moves across the layer with limited horizontal mixing [62]. In the burst-jet regime, we find $\mathrm{Nu} \sim (\mathrm{Ra}/\mathrm{Ra}_c)^{0.160}$ (dash-dot line), similar to the results of Ref. [37]. The zonal flows sweep the near-wall thermal plumes and inhibit heat transport across the layer.

[1] J. M. Aurnou and P. L. Olson, Experiments on Rayleigh-Bénard convection, magnetoconvection, and rotating magnetoconvection in liquid gallium, J. Fluid Mech. **430**, 283 (2001).

[2] E. M. King, S. Stellmach, J. Noir, U. Hansen, and J. M. Aurnou, Boundary layer control of rotating convection systems, Nature (London) **457**, 301 (2009).

[3] N. O. Weiss and M. Proctor, *Magnetoconvection* (Cambridge University Press, Cambridge, UK, 2014).

[4] R. E. Ecke and J. J. Niemela, Heat Transport in the Geostrophic Regime of Rotating Rayleigh-Bénard Convection, Phys. Rev. Lett. **113**, 114301 (2014).

[5] P. Garaud, B. Gallet, and T. Bischoff, The stability of stratified spatially periodic shear flows at low Péclet number, Phys. Fluids **27**, 084104 (2015).

[6] C. Guervilly and D. W. Hughes, Jets and large-scale vortices in rotating Rayleigh-Bénard convection, Phys. Rev. Fluids **2**, 113503 (2017).

[7] S. Horn and J. M. Aurnou, Regimes of Coriolis-Centrifugal Convection, Phys. Rev. Lett. **120**, 204502 (2018).

[8] M. K. Verma, *Physics of Buoyant Flows* (World Scientific, Singapore, 2018).

[9] J. S. Cheng, M. Madonia, A. J. Aguirre Guzmán, and R. P. J. Kunnen, Laboratory exploration of heat transfer regimes in rapidly rotating turbulent convection, Phys. Rev. Fluids **5**, 113501 (2020).

[10] M. Ghosh, P. Ghosh, Y. Nandukumar, and P. Pal, Transitions near the onset of low Prandtl-number rotating convection in presence of horizontal magnetic field, Phys. Fluids **32**, 024110 (2020).

[11] A. P. Ingersoll, Atmospheric dynamics of the outer planets, Science **248**, 308 (1990).

[12] D. H. Atkinson, J. B. Pollack, and A. Seiff, Galileo Doppler measurements of the deep zonal winds at Jupiter, Science **272**, 842 (1996).

[13] C. C. Porco, R. A. West, A. McEwen, A. D. Del Genio, A. P. Ingersoll, P. Thomas, S. Squyres, L. Dones, C. D. Murray, T. V. Johnson *et al.*, Cassini imaging of Jupiter's atmosphere, satellites, and rings, Science **299**, 1541 (2003).

[14] A. R. Vasavada and A. P. Showman, Jovian atmospheric dynamics: An update after Galileo and Cassini, Rep. Prog. Phys. **68**, 1935 (2005).

[15] N. Gómez-Pérez, M. Heimpel, and J. Wicht, Effects of a radially varying electrical conductivity on 3D numerical dynamos, Phys. Earth Planet. Inter. **181**, 42 (2010).

[16] M. Heimpel and N. Gómez Pérez, On the relationship between zonal jets and dynamo action in giant planets, Geophys. Res. Lett. **38**, 2005 (2011).

[17] M. French, A. Becker, W. Lorenzen, N. Nettelmann, M. Bethkenhagen, J. Wicht, and R. Redmer, Ab Initio simulations for material properties along the Jupiter adiabat, Astrophys. J. Suppl. Series **202**, 5 (2012).

[18] L. D. Duarte, T. Gastine, and J. Wicht, Anelastic dynamo models with variable electrical conductivity: An application to gas giants, Phys. Earth Planet. Inter. **222**, 22 (2013).

[19] H. Cao and D. J. Stevenson, Zonal flow magnetic field interaction in the semiconducting region of giant planets, Icarus (2017).

[20] S. M. Tobias, P. H. Diamond, and D. W. Hughes, β-plane magnetohydrodynamic turbulence in the solar tachocline, Astrophys. J. **667**, L113 (2007).

[21] S. M. Tobias, K. Dagon, and J. B. Marston, Astrophysical fluid dynamics via direct statistical simulation, Astrophys. J. **727**, 127 (2011).

[22] N. C. Constantinou and J. B. Parker, Magnetic suppression of zonal flows on a beta plane, Astrophys. J. **863**, 46 (2018).

[23] F. Wagner, A quarter-century of h-mode studies, Plasma Phys. Controlled Fusion **49**, B1 (2007).

[24] J. Wesson, *Tokamaks* (Oxford University Press, Oxford, UK, 2011).

[25] P. A. Davidson, *An Introduction to Magnetohydrodynamics* (Cambridge Univeristy Press, Cambridge, UK, 2001).

[26] M. K. Verma, Anisotropy in quasi-static magnetohydrodynamic turbulence, Rep. Prog. Phys. **80**, 087001 (2017).

[27] A. Pothérat and R. Klein, Do magnetic fields enhance turbulence at low magnetic Reynolds number? Phys. Rev. Fluids **2**, 063702 (2017).

[28] U. R. Christensen, P. Olson, and G. A. Glatzmaier, Numerical modelling of the geodynamo: A systematic parameter study, Geophys. J. Int. **138**, 393 (1999).

[29] F. H. Busse, Convective flows in rapidly rotating spheres and their dynamo action, Phys. Fluids **14**, 1301 (2002).

[30] J. Wicht, Inner-core conductivity in numerical dynamo simulations, Phys. Earth Planet. Inter., **132**, 281 (2002).

[31] T. Schneider and J. Liu, Formation of jets and equatorial superrotation on Jupiter, J. Atmos. Sci. **66**, 579 (2009).

[32] R. L. Kirk and D. J. Stevenson, Hydromagnetic constraints on deep zonal flow in the giant planets, Astrophys. J. **316**, 836 (1987).

[33] J. Liu, P. M. Goldreich, and D. J. Stevenson, Constraints on deep-seated zonal winds inside Jupiter and Saturn, Icarus **196**, 653 (2008), mars Polar Science IV.

[34] G. A. Glatzmaier, A note on "Constraints on deep-seated zonal winds inside Jupiter and Saturn," Icarus **196**, 665 (2008), mars Polar Science IV.

[35] M. Heimpel and J. M. Aurnou, Turbulent convection in rapidly rotating spherical shells: A model for equatorial and high latitude jets on Jupiter and Saturn, Icarus **187**, 540 (2007).

[36] T. Gastine, L. D. V. Duarte, and J. Wicht, Dipolar versus multipolar dynamos: The influence of the background density stratification, Astronomy Astrophysics **19**, 1 (2012).

[37] D. Goluskin, H. Johnston, G. R. Flierl, and E. A. Spiegel, Convectively driven shear and decreased heat flux, J. Fluid Mech. **759**, 360 (2014).

[38] J. Aubert, N. Gillet, and P. Cardin, Quasigeostrophic models of convection in rotating spherical shells, Geochemistry, Geophysics, Geosystems **4** (2003).

[39] M. A. Calkins, J. M. Aurnou, J. D. Eldredge, and K. Julien, The influence of fluid properties on the morphology of core turbulence and the geomagnetic field, Earth Planet. Sci. Lett. **359-360**, 55 (2012).

[40] T. Gastine, Pizza: an open-source pseudo-spectral code for spherical quasi-geostrophic convection, Geophys. J. Int. **217**, 1558 (2019).

[41] R. K. Scott and D. G. Dritschel, The structure of zonal jets in geostrophic turbulence, J. Fluid Mech. **711**, 576 (2012).

[42] Q. Wang, K. L. Chong, R. J. A. M. Stevens, R. Verzicco, and D. Lohse, From zonal flow to convection rolls in Rayleigh-Bénard convection with free-slip plates, J. Fluid Mech. **905**, A21 (2020).

[43] B. Favier, L. Silvers, and M. Proctor, Inverse cascade and symmetry breaking in rapidly rotating Boussinesq convection, Phys. Fluids **26**, 096605 (2014).

[44] K. Julien, E. Knobloch, and M. Plumley, Impact of domain anisotropy on the inverse cascade in geostrophic turbulent convection, J. Fluid Mech. **837**, R4 (2018).

[45] F. H. Busse, A simple model of convection in the Jovian atmosphere, Icarus **29**, 255 (1976).

[46] M. Heimpel and J. M. Aurnou, Convective bursts and the coupling of Saturn's equatorial storms and interior rotation, Astrophys. J. **746**, 51 (2012).

[47] E. J. Hopfinger, Turbulence in stratified fluids: A review, J. Geophys. Res. **92**, 5287 (1987).

[48] J. J. Riley and M.-P. Lelong, Fluid motions in the presence of strong stable stratification, Annu. Rev. Fluid Mech. **32**, 613 (2000).

[49] F. H. Busse, Convection driven zonal flows and vortices in the major planets, Chaos **4**, 123 (1994).

[50] U. R. Christensen, Zonal flow driven by deep convection in the major planets, Geophys. Res. Lett. **28**, 2553 (2001).

[51] A. P. Showman, Y. Kaspi, and G. R. Flierl, Scaling laws for convection and jet speeds in the giant planets, Icarus **211**, 1258 (2011).

[52] R. Simitev and F. H. Busse, Prandtl-number dependence of convection-driven dynamos in rotating spherical fluid shells, J. Fluid Mech. **532**, 365 (1999).

[53] C. A. Jones and P. H. Roberts, Convection-driven dynamos in a rotating plane layer, J. Fluid Mech. **404**, 311 (2000).

[54] J. Aubert, J. Aurnou, and J. Wicht, The magnetic structure of convection-driven numerical dynamos, Geophys. J. Int. **172**, 945 (2008).

[55] K. M. Soderlund, M. H. Heimpel, E. M. King, and J. M. Aurnou, Turbulent models of ice giant internal dynamics: Dynamos, heat transfer, and zonal flows, Icarus **224**, 97 (2013).

[56] M. A. Calkins, K. Julien, S. M. Tobias, and J. M. Aurnou, A multiscale dynamo model driven by quasi-geostrophic convection, J. Fluid Mech. **780**, 143 (2015).

[57] Y. Nakagawa, An experiment on the inhibition of thermal convection by a magnetic field, Nature (London) **175**, 417 (1955).

[58] J. Sommeria and R. Moreau, Why, how, and when, MHD turbulence becomes two-dimensional, J. Fluid Mech. **118**, 507 (1982).

[59] S. Cioni, S. Chaumat, and J. Sommeria, Effect of a vertical magnetic field on turbulent Rayleigh-Bénard convection, Phys. Rev. E **62**, R4520 (2000).

[60] A. Pothérat, J. Sommeria, and R. Moreau, An effective two-dimensional model for MHD flows with transverse magnetic field, J. Fluid Mech. **424**, 75 (2000).

[61] S. Chakraborty, On scaling laws in turbulent magnetohydrodynamic Rayleigh-Benard convection, Physica D **237**, 3233 (2008).

[62] M. Yan, M. A. Calkins, S. Maffei, K. Julien, S. M. Tobias, and P. Marti, Heat transfer and flow regimes in quasi-static magnetoconvection with a vertical magnetic field, J. Fluid Mech. **877**, 1186 (2019).

[63] T. Vogt, J.-C. Yang, F. Schindler, and S. Eckert, Free-fall velocities and heat transport enhancement in liquid metal magnetoconvection, J. Fluid Mech. **915**, A68 (2021).

[64] O. Zikanov, I. Belyaev, Y. Listratov, P. Frick, N. Razuvanov, and V. Sviridov, Mixed convection in pipe and duct flows with strong magnetic fields, Appl. Mech. Rev. **73**, 010801 (2021).

[65] Y. Xu, S. Horn, and J. M. Aurnou, Thermoelectric precession in turbulent magnetoconvection, J. Fluid Mech. **930**, A8 (2022).

[66] P. H. Roberts, *Introduction to Magnetohydrodynamics* (Longmans, Green and Co., London, UK, 1967).

[67] B. Knaepen, S. Kassinos, and D. Carati, Magnetohydrodynamic turbulence at moderate magnetic Reynolds number, J. Fluid Mech. **513**, 199 (1999).

[68] B. Knaepen and R. Moreau, Magnetohydrodynamic turbulence at low magnetic Reynolds number, Annu. Rev. Fluid Mech. **40**, 25 (2008).

[69] U. Schumann, Numerical simulation of the transition from three-to two-dimensional turbulence under a uniform magnetic field, J. Fluid Mech. **74**, 31 (1976).

[70] A. Pothérat and R. Klein, Why, how and when MHD turbulence at low *Rm* becomes three-dimensional, J. Fluid Mech. **761**, 168 (2014).

[71] G. Glatzmaier, *Introduction to Modeling Convection in Planets and Stars: Magnetic Field, Density Stratification, Rotation* (Princeton University Press, Princeton, NJ, 2014).

[72] K. J. Burns, G. M. Vasil, J. S. Oishi, D. Lecoanet, and B. P. Brown, Dedalus: A flexible framework for numerical simulations with spectral methods, Phys. Rev. Res. **2**, 023068 (2020).

[73] S. Chandrasekhar, *Hydrodynamic and Hydromagnetic Stability* (Oxford University Press, Oxford, UK, 1961).

[74] M. Proctor and N. Weiss, Magnetoconvection, Rep. Prog. Phys. **45**, 1317 (1982).

[75] P. Matthews, Asymptotic solutions for nonlinear magnetoconvection, J. Fluid Mech. **387**, 397 (1999).

[76] O. Shishkina, M. S. Emran, S. Grossmann, and D. Lohse, Scaling relations in large-Prandtl-number natural thermal convection, Phys. Rev. Fluids **2**, 103502 (2017).

[77] B. Sreenivasan and T. Alboussière, Experimental study of a vortex in a magnetic field, J. Fluid Mech. **464**, 287 (2002).
[78] T. Zürner, Refined mean field model of heat and momentum transfer in magnetoconvection, Phys. Fluids **32**, 107101 (2020).
[79] D. Nieves, A. M. Rubio, and K. Julien, Statistical classification of flow morphology in rapidly rotating Rayleigh-Bénard convection, Phys. Fluids **26**, 086602 (2014).
[80] S. Stellmach, M. Lischper, K. Julien, G. Vasil, J. S. Cheng, A. Ribeiro, E. M. King, and J. M. Aurnou, Approaching the Asymptotic Regime of Rapidly Rotating Convection: Boundary Layers Versus Interior Dynamics, Phys. Rev. Lett. **113**, 254501 (2014).
[81] R. P. J. Kunnen, The geostrophic regime of rapidly rotating turbulent convection, J. Turbul. **22**, 267 (2021).
[82] M. Madonia, A. J. A. Guzmán, H. J. Clercx, and R. P. Kunnen, Velocimetry in rapidly rotating convection: Spatial correlations, flow structures and length scales (a), Europhys. Lett. **135**, 54002 (2021).
[83] S. Grossmann and D. Lohse, Scaling in thermal convection: A unifying theory, J. Fluid Mech. **407**, 27 (2000).
[84] T. Zürner, W. Liu, D. Krasnov, and J. Schumacher, Heat and momentum transfer for magnetoconvection in a vertical external magnetic field, Phys. Rev. E **94**, 043108 (2016).
[85] A. Rucklidge and P. Matthews, Analysis of the shearing instability in nonlinear convection and magnetoconvection, Nonlinearity **9**, 311 (1996).
[86] S. Paul, M. K. Verma, P. Wahi, S. K. Reddy, and K. Kumar, Bifurcation analysis of the flow patterns in two-dimensional Rayleigh–Bénard convection, Int. J. Bifurcation Chaos **22**, 1230018 (2012).
[87] U. Hansen, D. A. Yuen, and S. E. Kroening, Transition to hard turbulence in thermal convection at infinite Prandtl number, Phys. Fluids **2**, 2157 (1990).
[88] M. Manga and D. Weeraratne, Experimental study of non-Boussinesq Rayleigh-Bénard convection at high Rayleigh and Prandtl numbers, Phys. Fluids **11**, 2969 (1999).
[89] S. Horn, O. Shishkina, and C. Wagner, On non-Oberbeck-Boussinesq effects in three-dimensional Rayleigh-Bénard convection in glycerol, J. Fluid Mech. **724**, 175 (2013).
[90] N. Cagney, W. H. Newsome, C. Lithgow-Bertelloni, A. Cotel, S. R. Hart, and J. A. Whitehead, Temperature and velocity measurements of a rising thermal plume, Geochemistry, Geophysics, Geosystems **16**, 579 (2015).
[91] P. Terry, Suppression of turbulence and transport by sheared flow, Rev. Mod. Phys. **72**, 109 (2000).
[92] M. Cross and H. Greenside, *Pattern Formation and Dynamics in Nonequilibrium Systems* (Cambridge University Press, Cambridge, UK, 2009).
[93] C. A. Jones, Convection–driven geodynamo models, Philos. Trans. R. Soc. London A **358**, 873 (2000).
[94] B. Sreenivasan and C. A. Jones, Structure and dynamics of the polar vortex in the Earth's core, Geophys. Res. Lett. **32**L20301 (2005).
[95] J. M. Aurnou, S. Andreadis, L. Zhu, and P. L. Olson, Experiments on convection in Earth's core tangent cylinder, Earth Planet. Sci. Lett. **212**, 119 (2003).
[96] S. Stanley and G. A. Glatzmaier, Dynamo models for planets other than Earth, Space Sci. Rev. **152**, 617 (2010).
[97] T. Gastine and J. Wicht, Effects of compressibility on driving zonal flow in gas giants, Icarus **219**, 428 (2012).
[98] A. P. Showman, P. J. Gierasch, and Y. Lian, Deep zonal winds can result from shallow driving in a giant-planet atmosphere, Icarus **182**, 513 (2006), results from the Mars Express ASPERA-3 Investigation.
[99] K. Zhang, D. Kong, and G. Schubert, Thermal-gravitational wind equation for the wind-induced gravitational signature of giant gaseous planets: Mathematical derivation, numerical method, and illustrative solutions, Astrophys. J. **806**, 270 (2015).
[100] D. Kong, K. Zhang, G. Schubert, and J. D. Anderson, Origin of Jupiter's cloud-level zonal winds remains a puzzle even after Juno, Proc. Natl. Acad. Sci. USA **115**, 8499 (2018).
[101] M. Heimpel, J. Aurnou, and J. Wicht, Simulation of equatorial and high-latitude jets on Jupiter in a deep convection model, Nature (London) **438**, 193 (2005).
[102] J. Liu, T. Schneider, and Y. Kaspi, Predictions of thermal and gravitational signals of Jupiter's deep zonal winds, Icarus **224**, 114 (2013).
[103] U. R. Christensen, J. Wicht, and W. Dietrich, Mechanisms for limiting the depth of zonal winds in the gas giant planets, Astrophys. J. **890**, 61 (2020).
[104] Y. Kaspi, E. Galanti, A. P. Showman, D. J. Stevenson, T. Guillot, L. Iess, and S. J. Bolton, Comparison of the deep atmospheric dynamics of Jupiter and Saturn in light of the Juno and Cassini gravity measurements, Space Sci. Rev. **216**, 84 (2020).
[105] C. A. Jones, A dynamo model of Jupiter's magnetic field, Icarus **241**, 148 (2014).
[106] K. M. Soderlund, E. M. King, and J. M. Aurnou, The influence of magnetic fields in planetary dynamo models, Earth Planet. Sci. Lett. **333-334**, 9 (2012).
[107] E. M. King and J. M. Aurnou, Magnetostrophic balance as the optimal state for turbulent magnetoconvection, Proc. Natl. Acad. Sci. USA **112**, 990 (2015).
[108] J. M. Aurnou and E. M. King, The cross-over to magnetostrophic convection in planetary dynamo systems, Proc. R. Soc. A: Math., Phys. Eng. Sci. **473**, 20160731 (2017).
[109] R. J. Orvedahl, N. A. Featherstone, and M. A. Calkins, Large-scale magnetic field saturation and the Elsasser number in rotating spherical dynamo models, Monthly Notices R. Astron. Soc.: Lett. **507**, L67 (2021).
[110] J. E. P. Connerney, S. Kotsiaros, R. J. Oliversen, J. R. Espley, J. L. Joergensen, P. S. Joergensen, J. M. G. Merayo, M. Herceg, J. Bloxham, K. M. Moore, S. J. Bolton, and S. M. Levin, A new model of Jupiter's magnetic field from Juno's first nine orbits, Geophys. Res. Lett. **45**, 2590 (2018).
[111] B. Galperin, R. M. Young, S. Sukoriansky, N. Dikovskaya, P. L. Read, A. J. Lancaster, and D. Armstrong, Cassini observations reveal a regime of zonostrophic macroturbulence on Jupiter, Icarus **229**, 295 (2014).
[112] S. Maffei, M. A. Calkins, K. Julien, and P. Marti, Magnetic quenching of the inverse cascade in rapidly rotating convective turbulence, Phys. Rev. Fluids **4**, 041801(R) (2019).
[113] Z. Yu, H. Leinweber, and C. Russell, Galileo constraints on the secular variation of the Jovian magnetic field, J. Geophys. Res.: Planets **115**, E03002 (2010).

[114] V. A. Ridley and R. Holme, Modeling the Jovian magnetic field and its secular variation using all available magnetic field observations, J. Geophys. Res.: Planets **121**, 309 (2016).

[115] Y. Kaspi, E. Galanti, W. B. Hubbard, D. J. Stevenson, S. J. Bolton, L. Iess, T. Guillot, J. Bloxham, J. E. P. Connerney, H. Cao, D. Durante, W. M. Folkner, R. Helled, A. P. Ingersoll, S. M. Levin, J. I. Lunine, Y. Miguel, B. Militzer, M. Parisi, and S. M. Wahl, Jupiter's atmospheric jet streams extend thousands of kilometres deep, Nature (London) **555**, 223 (2018).

[116] M. Schöttler and R. Redmer, *Ab Initio* Calculation of the Miscibility Diagram for Hydrogen-Helium Mixtures, Phys. Rev. Lett. **120**, 115703 (2018).

[117] T. Gastine and J. Wicht, Stable stratification promotes multiple zonal jets in a turbulent Jovian dynamo model, Icarus **368**, 114514 (2021).